The Baryonic Matter and Geometry of the Local Group

by

Thorold Tronrud
B.Sc., University of Chicago, 2016

A Thesis Submitted in Partial Fulfillment of the
Requirements for the Degree of

MASTER OF SCIENCE

in the Department of Physics and Astronomy

The Baryonic Matter and Geometry of the Local Group

by

Thorold Tronrud
B.Sc., University of Chicago, 2016

Supervisory Committee

Dr. J. F. Navarro, Supervisor
(Department of Physics and Astronomy)

Dr. K. Venn, Departmental Member
(Department of Physics and Astronomy)

ABSTRACT

First, the baryonic content of simulated halos of virial masses between $5 \times 10^9 M_\odot$ to $5 \times 10^{12} M_\odot$ in the APOSTLE project is examined in the context of the missing baryon problem. Baryonic particles in APOSTLE can be either stars or gas. Non-star-forming gas, or the circumgalactic medium (CGM) is further classified by temperature into the Cool CGM (CCGM, $T < 10^5 K$), or the Warm-Hot CGM (WHCGM, $T > 10^5 K$). APOSTLE halos are found to contain less than 60% of the expected mass of baryons ($f_b = \Omega_b/\Omega_m$, $M_b = f_b \times M_{200}$) within their virial radius. The WHCGM contains 29% ± 10%, the CCGM 12% ± 5%, and the stars and star-forming gas 19% ± 5%. The metal content of the same halos is analyzed, and compared to the total metals produced by the stars within the virial radius. Over two thirds of the produced metals are retained within the halo, with 14% ± 3% in the WHCGM, 13% ± 4% in the CCGM, and 43% ± 9% in the stars and star-forming gas.

Next, we focus on the overall distribution of matter within a $3Mpc$ radius from the Milky Way. Using the trends in APOSTLE volumes, I quantify both the ellipticity and orientation of this spatial distribution using the principal axes of the inertia tensor of the positions of these galaxies. The Zone of Avoidance has little impact on this result, and the short axis is aligned with that of the Supergalactic Plane, and is perpendicular to the vector separating the Milky Way and Andromeda galaxies. APOSTLE local group analogues are found to be similarly anisotropic, and like in the observed Local Group, the minor axis of that distribution is found to be perpendicular to the vector separating the two primaries. The angular momentum of the stellar disk shows weak alignment with the minor axis of the field galaxy distribution. In addition the simulations also suggest that the angular momenta of the two primary dark-matter halos tend to be anti-aligned. Additionally, stellar disks tend to orient themselves in the same direction as their halo.

Contents

List of Tables

List of Figures

Acknowledgements

I would like to thank:

My parents, and my friends for keeping me sane.

Julio Navarro, for mentorship, support, encouragement, and much patience.

Kyle Oman, for writing the Python backbone that keeps our research group upright.

Azadeh Fattahi, for her unending patience while answering my dumb questions.

Dr. F. Munshi, the external examiner.

Dedication

Just hoping this is useful!

Chapter 1

Introduction

1.1 The Standard Model of Cosmology

The current paradigm of cosmology, called Λ Cold Dark Matter (ΛCDM, where Λ refers to the dark energy component), is a direct result of the rise of precision cosmology, heralded by large-scale redshift surveys, and observations of the cosmic microwave background (CMB). ΛCDM is made up of several theories of the evolution and makeup of the Universe. First, the Universe begins with a hot big bang. In the preceding few minutes, space is hot and dense enough for nucleosynthesis (BBN, or Big Bang Nucleosynthesis) to take place. This produces primordial abundances of ^1H, ^2H, ^3He, ^4He, and ^7Li that can be used to constrain the baryon density of the universe (Walker et al., 1991[1]). The total energy of the universe is divided between baryonic matter, which is what makes up the observed Universe, non-baryonic CDM, and Λ. The initial seeds of galaxies were quantum fluctuations in the density field of the early universe, which grew hierarchically through mergers.

The expansion rate of the universe is given by $H(t) \equiv \dot{a}(t)/a(t)$, where $a(t)$ is the scale of the universe with respect to the current epoch (referred to as a_0), and $\dot{a}(t)$ is its time derivative. The Friedmann equation (Friedmann, 1922[2]) describes the evolution of H as:

$$\frac{H(t)^2}{H_0^2} = \Omega_\Lambda + \frac{1-\Omega_0}{a(t)^2} + \frac{\Omega_m}{a(t)^3} + \frac{\Omega_r}{a(t)^4} \tag{1.1}$$

H_0 is the Hubble Constant, and is defined as $100hkm/s/Mpc$. Ω_Λ, Ω_m, and Ω_r are the current densities of dark energy, gravitating matter, and radiation in units of the energy density of a flat universe, where the total energy density is equal to the critical

density.[1] Ω_0 is the sum of every density term, and dictates the shape of the universe, with $\Omega_0 = 1$ representing a flat cosmology. Should the Universe be less dense than the critical density ($\Omega_0 < 1$), the self-gravity of the universe is unable to halt the expansion, and parallel light rays will eventually diverge. If $\Omega_0 > 1$, the expansion of the Universe will slow and eventually stop, before it falls back in on itself, and initially parallel light rays will converge to a point.

1.2 Cosmological Interpretations of the WMAP-7 Observations

The cosmic microwave background (CMB) plays a pivotal role in efforts to constrain the cosmological parameters, and is the result of the decoupling of matter and radiation once the universe cooled enough for neutral hydrogen to form. Minute differences in CMB photon temperature across the sky can be used to derive parameters independent of redshift surveys.

By combining 7-year data from the Wilkinson Microwave Anisotropy Probe (WMAP) with improved astrophysical data from Baryon Acoustic Oscillation (BAO) measurements, and Hubble constant measurements, the 6 parameters of the simplest ΛCDM model can be determined (Komatsu et al., 2010[3]). Values such as H_0, Ω_m, and Ω_b can be derived from the primary parameters. The values of these that were used as the initial conditions in the simulations presented throughout this thesis are $\Omega_m = 0.272$, $\Omega_b = 0.0455$, $\Omega_\Lambda = 0.728$, and $H_0 = 70.4 km/s/Mpc$ (presented in Table 1.1).

1.3 Galaxies and Halos in ΛCDM

From the initial fluctuations in the density field, small clumps of matter merge to form hierarchically larger structures. Large dark matter halos grow through accretion of smaller objects and mergers with other massive halos. White and Rees (1978[4]) describe how the baryonic matter, which makes up much less of the total mass, fell into the gravitational potential of the dark matter, where it could condense into gas clouds and form galaxies. These halos can only be detected by their gravitational effects, which means that the largest halos with the strongest forces are the easiest to detect.

[1] $\rho_c = \frac{3H^2}{8\pi G}$, where G is Newton's gravitational constant.

Since dark matter is distributed across all space in the Universe, the extent of a halo is given as a radius that encloses a certain density. In this thesis, I will use R_{200} and M_{200}, which correspond to the radius that encloses a density of 200 times the critical density of the Universe, and to the enclosed mass. This means that

$$M_{200} = 200 \times \frac{4}{3}\pi R_{200}^3 \rho_c \tag{1.2}$$

1.4 The Circumgalactic Medium

Results from WMAP-7 indicate that, on cosmological scales, the mass ratio of baryons to dark matter is $\Omega_b/\Omega_m \approx 0.17$. The observed mass of cold gas and stars within galactic halos accounts for less than 10% of this expected fraction (Fukugita et al., 1998[5]; McGaugh et al., 2009[6]; Wang et al., 2017[7]). Instead, the majority of a galaxy's baryonic mass is expected to be at high temperatures and contiguous with the intergalactic medium. (Cen & Ostriker, 1999[8]; Wang et al., 2017[7]). Within the virial radius of a galaxy, this non-star forming gas is referred to as the circumgalactic medium (CGM). The COS survey has estimated that the mass of the cool CGM ($T < 10^5 K$) in Milky Way-like halos accounts for 30-50% of the expected baryonic mass (Werk et al., 2014[9]), with additional mass contribution from CGM gas at even higher temperatures.

Simulations have supported the paradigm that a majority of the baryonic mass in a halo is made up of hot, diffuse gas (Dav, 2009[10]; Sokoowska et al., 2016[11]). For example, in the Eris suite of cosmological simulations (Guedes et al., 2011[12]), gas with a temperature below $10^5 K$ is more centrally concentrated than gas above this limit. The hotter gas, above $10^5 K$ comprises the majority of baryons within $0.2R_{200}$. In total, this hot phase of gas accounts for roughly 80% of the total gas reservoir within the halo (Sokoowska et al., 2016[11]).

In the Eagle Simulations (Schaye et al., 2015[13]), warm-hot CGM ($T > 10^5 K$) gas only dominates the baryonic mass of the halo until approximately $0.5R_{200}$, In total, this gas makes up nearly a third of the expected baryonic mass in Milky Way-sized halos(Oppenheimer et al., 2018[14]), which is in agreement with the results of the Eris simulations. The cool ($T < 10^5 K$) CGM gas also forms a significant component of the baryonic mass surrounding these galaxies, in both sets of simulations.

The balance between cool and warm-hot CGM components is determined by halo mass. The NIHAO simulations (Wang et al., 2015[15]; Wang et al., 2017[7]) predict that Milky Way-size halos should be dominated by the warm-hot CGM. In this work, we extend this analysis to the APOSTLE simulations.

1.5 The Local Group of Galaxies

For the purposes of this thesis, the Local Group (LG) corresponds to the galaxies within a 3Mpc sphere around the Milky Way (MW). The Andromeda galaxy (M31) is the nearest large galaxy, at a distance of approximately 800 kpc. The next-nearest large galaxy, M82, is roughly 3.5Mpc away (Karachentsev and Kashibadze, 2005[16]), leaving the MW-M31 system very isolated. The analysis presented in this thesis is based on a catalogue of nearby galaxies compiled from the Extragalactic Distance Database (EDD, Tully et al., 2009[17]). Dwarf galaxies in the LG system are either satellites of the Milky Way or Andromeda, or lie far away from either.

Galaxies that are further than 300kpc from either the Milky Way or M31 galaxies, but are also within 3 Mpc of the Milky Way will be referred to in this thesis as "Local Group field dwarfs". The LG Field Dwarfs selected for this thesis must also have a stellar mass greater than $10^5 M_\odot$, calculated using the Solar mass-to-light ratio in the wavelengths of light available in the EDD.

1.6 Numerical Simulations

The physics of the ΛCDM universe is extremely complex, so simulations provide important studies of cosmological behaviour. Given initial conditions, these programs integrate over time, based on the physics that are being modeled (eg. gravity). Matter is treated as a fluid in astrophysical contexts, and in this thesis, the simulations I will be dealing with use particle-based methods of solving hydrodynamics equations, covered in Section 1.6.2.

1.6.1 Dark Matter in Simulations

Since dark matter makes up over 80% (Table 1.1) of the total mass of the Universe, cosmological structure formation is driven by the merging and accretion of halos. In the simulations suite used in this thesis, dark matter is treated as a collisionless fluid that only interacts gravitationally with other matter. This simple model of 5/6th of our Universe's mass has allowed for extremely large scale simulations, such as the Millenium Run (Springel et al., 2005[18]) to take place.

1.6.2 Hydrodynamics in Simulations

In order to accurately model galaxy formation, it is necessary to include baryonic physics in the simulations. It is impossible to simulate all the baryons in a simulation, which means that a spatial scale must be imposed. Any process that takes place on a scale smaller than this is "subgrid" physics, and is calculated in simulations with pre-defined prescriptions. Such subgrid physics includes feedback, star formation, gas cooling, and the UV-XRay background radiation. The parameters associated with these are assumed differently in each research group (Schaye et al., 2015[13]; Vogelsberger et al., 2014[19]; Hopkins et al., 2017[20]; Wang et al., 2015[15]; Wadsley et al., 2017[21]), and are tuned such that the simulation reproduces observed global properties.

Perhaps even more of a problem than the immense time required to calculate the hydrodynamic quantities and their effects, is the fact that the full form of the governing equations is unknown. This means that results vary between different methods and researchers. Scannapieco et al. (2012[22]) demonstrated that each major simulation code, when provided with the same initial conditions, yields drastically different galaxies, which highlights the amount of uncertainty within the field.

This thesis is based on a suite of simulations that use smooth-particle hydrodynamics. This is characterized by treating particles as spherical clouds, with a known radial density dependence, called the kernel. For instance, the commonly-used Wendlend C^2 kernel is defined as:

$$W(q) = \alpha_d(1 - q/2)^4(2q + 1) \tag{1.3}$$

Within values of $0 \leq q \leq 2$, where $\alpha_d = \frac{21}{16\pi h^3}$ for 3-dimensional kernels, h is the smoothing length of the kernel, and q is distance from the central point in terms of the smoothing length.

1.6.3 Zoom-In Simulations

Often, one wants to simulate a specific region in detail, while retaining the much larger cosmological context that the region evolves within. Regions of interest are selected from a large, low-resolution simulation. The simulation is then re-run with the volume of interest filled with the desired spatial or mass resolution. Since tidal forces will be preserved on the large scale, the zoomed region will behave similarly to its low-resolution predecessor.

1.7 The APOSTLE Simulations

The APOSTLE (A Project of Simulations of the Local Environment) simulations are a set of 12 zoom-in volumes chosen from the DOVE dark-matter-only simulation (Jenkins, 2013[23]) to match the environmental circumstances of our own Local Group, with the WMAP-7 cosmological parameters (Covered in Section 1.2). The chosen volumes contain an isolated pair of halos of $M_{200} \approx 10^{12} M_\odot$, separated by 600-1000 kpc, and with a radial velocity between 0-250 km/s. Tangential velocity was also constrained below 100 km/s. Each volume is also uncontaminated by boundary particles within roughly 3 Mpc of the pair's barycentre.

Three resolution levels were simulated using code developed for the EAGLE project (Schaye et al. 2015[13]; Crain et al. 2015[24]). This code consists of a heavily-modified Gadget-3 (Springel 2005[25]), which utilises the pressure-entropy formalism for hydrodynamics calculations developed by Hopkins (2013[26]).

The subgrid models were tuned to match the observed stellar mass function of galaxies at z = 0.1, between $10^8 M_\odot < M^* < 10^{12} M_\odot$. Details of the subgrid models can be found in Schaye et al. (2015[13]) and Crain et al. (2015[24]).

The APOSTLE simulations implement a Chabrier initial mass function (IMF,Chabrier, 2003[27]). Star particles inherit the kernel-smoothed abundances of their progenitor

gas particles, which are then used to calculate their yields. The use of smoothed metallicities, where the metal content of a particle is combined with those within its smoothing radius, simulates the mixing of metals in the gas.

In order to prevent artificial fragmentation of the interstellar medium (ISM), the gas particles are not allowed to cool past a temperature floor imposed by a polytropic equation of state normalized to $3 \times 10^8 K$ at a density of $n_H = 10^{-1} cm^{-3}$.

Halos and subhalos are found in the volumes with the friends-of-friends (FoF) algorithm (Davis et al. 1985[28]), and SUBFIND (Springel et al. 2001[29]). FoF first examines the dark matter particles, using a linking length of one-fifth the mean inter-particle separation. Gas and star particles are then associated with the FoF group of the nearest dark matter particle. SUBFIND then searches through the FoF groups to find any sub-grouping of any particle type associated with the halo. The M31 and MW analogues in each volume are referred to as the "primaries", or "primary" and "secondary" in each volume, though in some they are in the same FoF group.

The three different resolution levels correspond to three different lower bounds on particle mass. L3, the lowest resolution, has a gas particle mass of roughly $1.5 \times 10^6 M_\odot$, with a gravitational softening radius of 711 pc. L2, the medium resolution, has a minimum mass of approximately $1 \times 10^5 M_\odot$, and a softening distance of 307 pc. Finally, L1, the highest resolution, has a particle mass of $1 \times 10^4 M_\odot$, and a smoothing radius of 134 pc.

This thesis will primarily use the medium-resolution L2 simulations, which encompass all 12 chosen volumes. The mass resolutions are provided in Table 1.2. The medium resolution was selected because simulations exist at this level for all volumes (high resolution results are only available for several), and the lower bound on LG Field Dwarf mass means that the galaxies considered can be resolved in the simulations.

The diversity of APOSTLE Local Group-analogues is apparent when they are viewed in sequence, as in Figures 1.1 to 1.4. The information pertaining to each individual volume is given in Table 1.2:

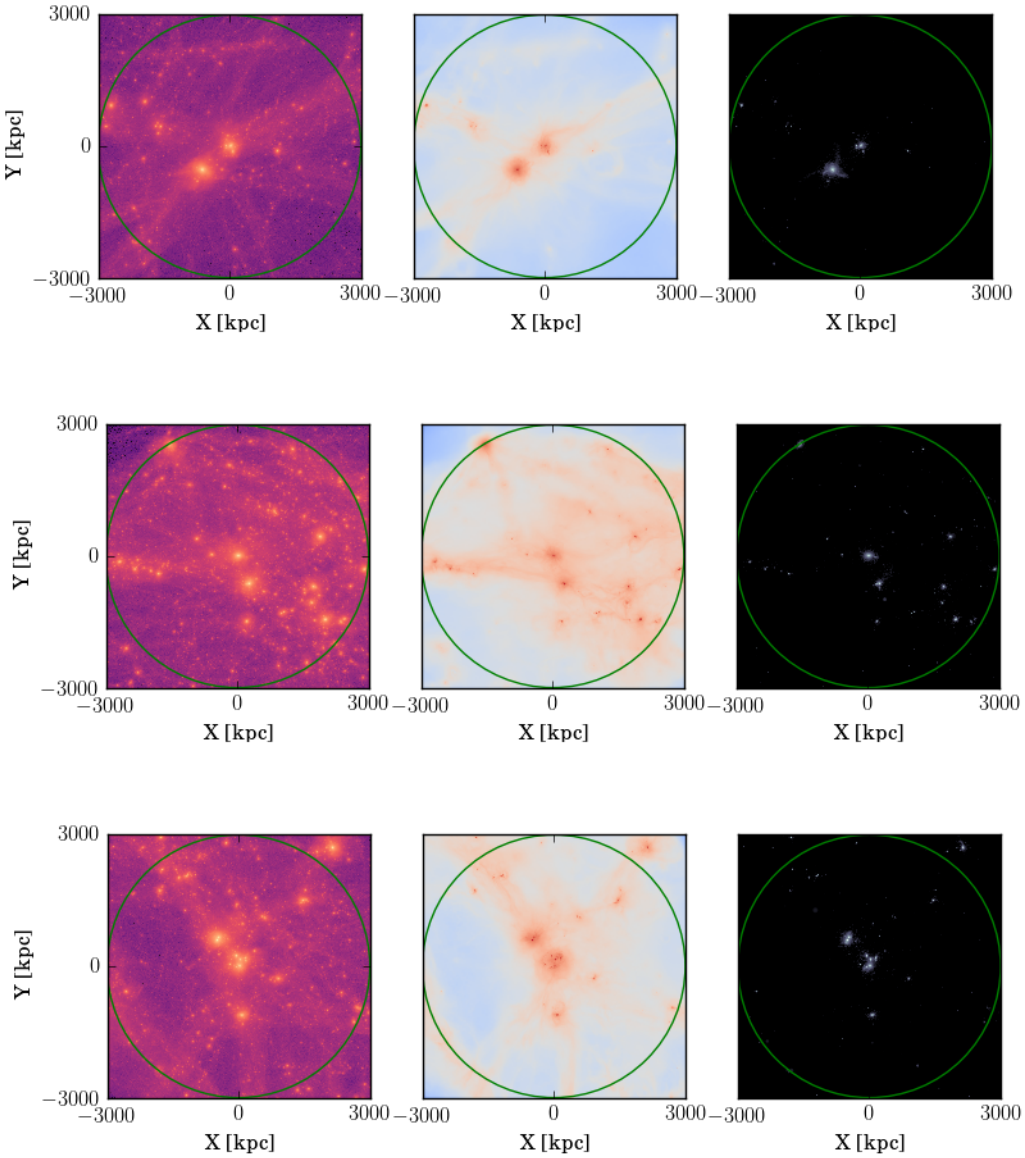

Figure 1.1: APOSTLE L2 Volumes 1 to 3, from left to right: Dark Matter, Gas, and Star particles.

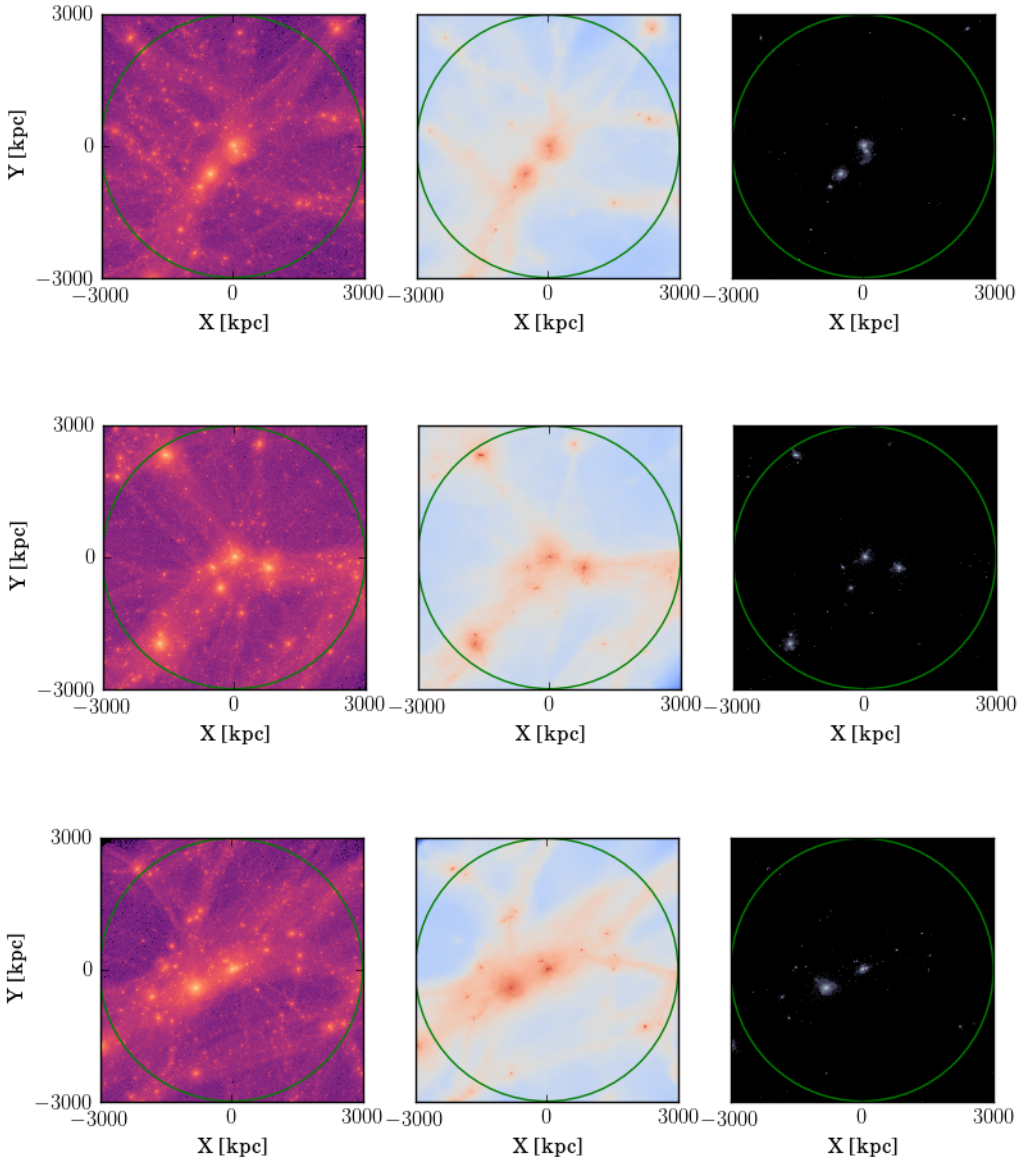

Figure 1.2: APOSTLE L2 Volumes 4 to 6, from left to right: Dark Matter, Gas, and Star particles.

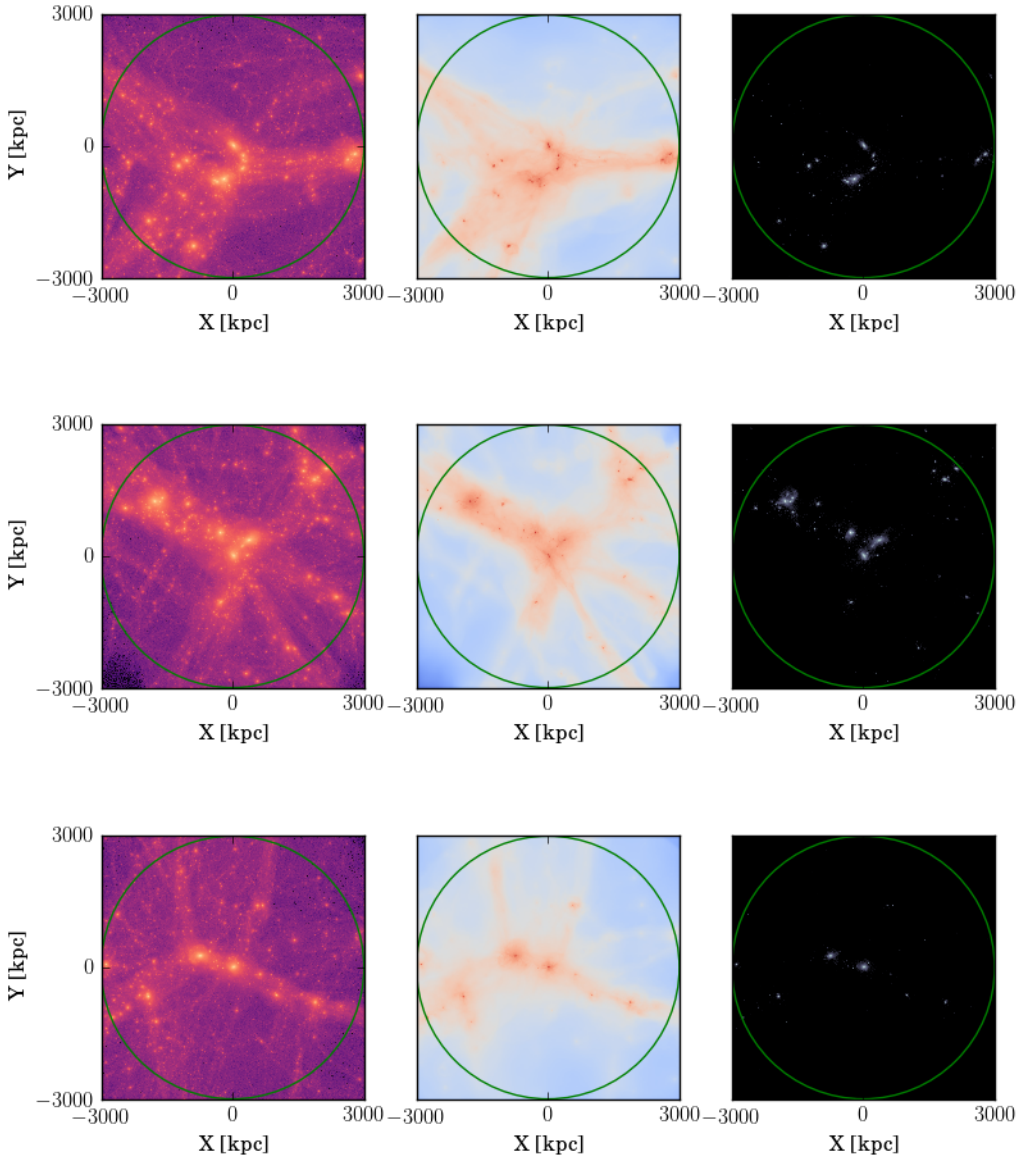

Figure 1.3: APOSTLE L2 Volumes 7 to 9, from left to right: Dark Matter, Gas, and Star particles.

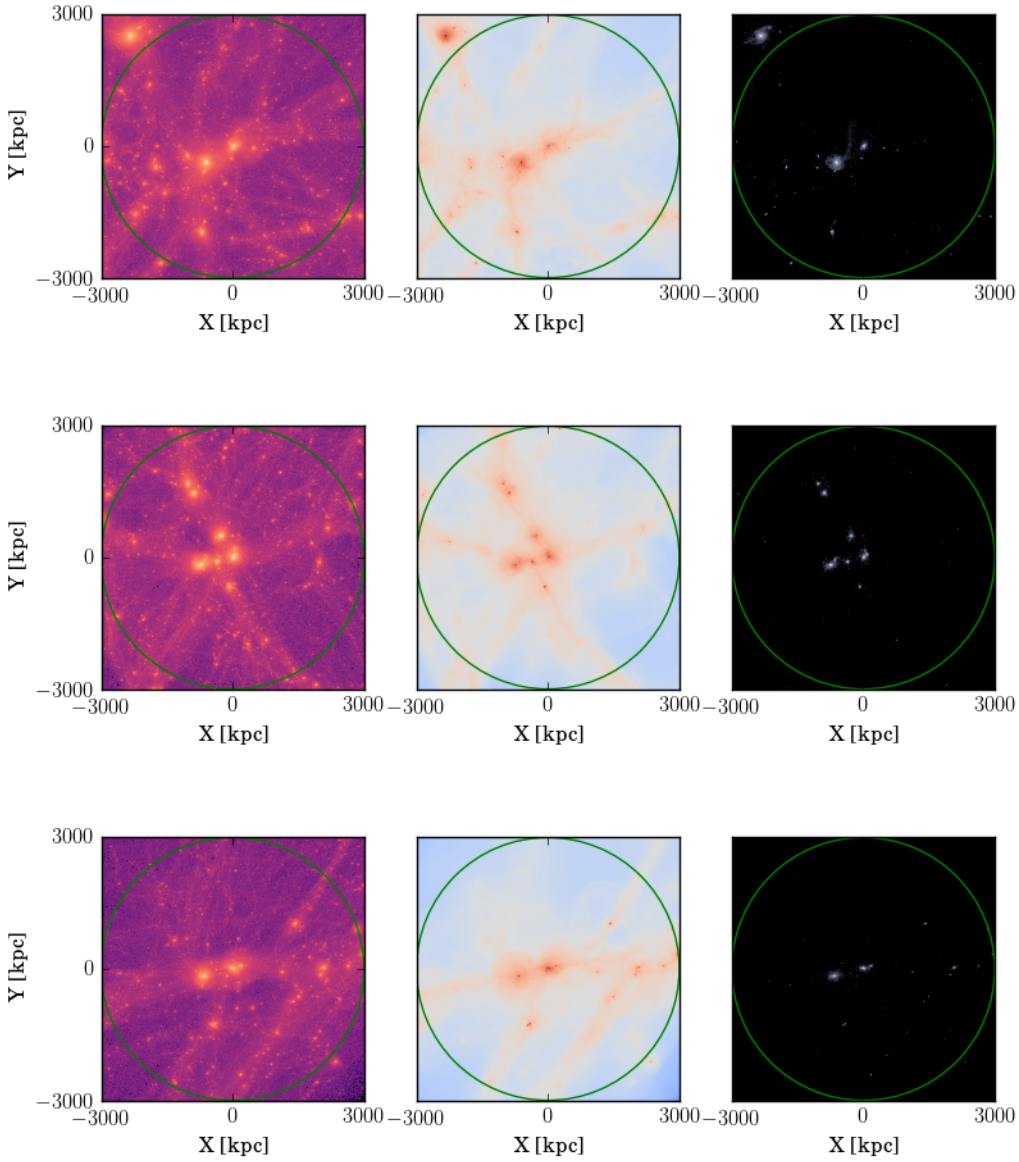

Figure 1.4: APOSTLE MR Volumes 10 to 12, from left to right: Dark Matter, Gas, and Star particles.

Table 1.1: WMAP-7 cosmological parameters used in the APOSTLE simulations

Parameter	Value
Ω_m	0.272
Ω_b	0.0455
Ω_Λ	0.728
H_0	70.4 km/s/Mpc
σ_8	0.81
n_s	0.967

Name	Resolutions	$M_{200}^{[1]}$	$M_{200}^{[2]}$	Separation [kpc]	V_r [km/s]	V_t [km/s]	M_{gas} [$10^4 M_\odot$]	ϵ_{max} [pc]
AP1	L1/L2/L3	1.66	1.10	850	51	35	0.99/12.0/147	134/307/711
AP2	L2/L3	0.85	0.83	809	39	97	12.5/147	307/711
AP3	L2/L3	1.52	1.22	920	35	84	12.5/147	307/711
AP4	L1/L2/L3	1.38	1.35	790	59	24	0.49/12.2/147	134/307/711
AP5	L2/L3	0.93	0.87	828	33	101	12.5/147	307/711
AP6	L2/L3	2.36	1.21	950	18	60	12.7/137	307/711
AP7	L2/L3	1.88	1.09	664	174	24	11.3/134	307/711
AP8	L2/L3	1.72	0.65	817	120	96	11.0/137	307/711
AP9	L2/L3	0.96	0.68	814	28	48	10.9/138	307/711
AP10	L2/L3	1.46	0.87	721	63	48	11.0/146	307/711
AP11	L2/L3	0.99	0.80	770	124	22	11.1/153	307/711
AP12	L2/L3	1.11	0.58	635	53	50	10.9/138	307/711

Table 1.2: APOSTLE simulation volume information. Virial parameters associated to the primary or secondary halo are labelled with [1] or [2]. The radial and tangential velocities of the halos are given, as are the gas particle mass, and gravitational smoothing radius.

1.8 Thesis Outline

In this thesis I will be studying the distribution of baryonic matter in the context of our Local Group. As observed through stars, and partially-photoinonized cold gas, the mass of the Milky Way is $6.5 \times 10^{10} M_{\odot}$. However the total baryonic and dark matter mass is approximately $1 - 2 \times 10^{12} M_{\odot}$, which would mean the Milky Way only has roughly a fifth of the expected cosmological mass of baryons (Nicastro et al., 2016[30]). Is this estimation of baryonic mass correct in ΛCDM? If so, then where are the ejected baryons in the Local Group? If not, then what state are the unobserved baryons in?

In chapter 2, I examine the retention of baryons and metals within the virial radius[2] of APOSTLE LG galaxies. The non-star forming gas within the virial radius, referred to as the circumgalactic medium, is separated by temperature into cooler and hotter categories. Average temperature, density, radial velocity, and cumulative mass profiles for the 24 APOSTLE primary galaxies are presented, and compared with previous models. In addition, metallicity of each category is compared with that of the rest of the galaxy.

Chapter 3 focuses primarily on the shape of the field dwarf galaxy distribution of the Local Group. This is examined in the context of the APOSTLE simulations, and the extended local environment, such as the Supergalactic Plane. This analysis is performed on the largest sample of LG Field Dwarfs to-date, and is used to refine estimates of the principal axes and eccentricity of the Field Dwarf distribution. Following that, the angular momenta of the disks of the APOSTLE primary galaxies are compared with the anisotropy of their local environment, so as to check whether the observed distribution of galaxies is consistent with ΛCDM.

Chapter 4 presents a brief conclusion, as well as possible avenues for future work.

[2]The virial radius corresponds to the radius that encloses a density of 200 times the critical density of the universe.

Chapter 2

Inventory of Baryons in Simulations of the Local Group

The baryonic content of simulated halos of virial masses between $5 \times 10^9 M_\odot$ to $5 \times 10^{12} M_\odot$ in the APOSTLE project is examined. Baryonic particles can be either stars or gas. Non-star-forming gas, or the circumgalactic medium (CGM) is further classified by temperature into the Cool CGM (CCGM, $T < 10^5 K$), or the Warm-Hot CGM (WHCGM, $T > 10^5 K$). APOSTLE halos are found to contain less than 60% of the expected mass of baryons ($f_b = \Omega_b/\Omega_m$, $M_b = f_b \times M_{200}$) within their virial radius. The WHCGM contains 29% ± 10%, the CCGM 12% ± 5%, and the stars and star-forming gas 19% ± 5%. The metal content of the same halos is analyzed, and compared to the total metals produced by the stars within the virial radius. Over two thirds of the produced metals are retained within the halo, with 14% ± 3% in the WHCGM, 13% ± 4% in the CCGM, and 43% ± 9% in the stars and star-forming gas.

2.1 Introduction

The early universe was a homogeneous mix of dark and baryonic matter. The mass ratio of these components can be determined by examining the power spectrum of the cosmic microwave background (see section 1.1). The WMAP-7 cosmological parameters predict this mass ratio of baryons to total matter to be $f_b = \Omega_b/\Omega_0 = 0.167$ (Komatsu et al., 2011[3]). In regions of space that are representative of the Universe, such as galaxy clusters, the baryonic mass contained within the virial radius (r_{200})[1] of a dark matter halo contains $M_b = f_b \times M_{200}$ mass in baryons (White et al., 1993[31]).

[1]The virial radius corresponds to the radius that encloses a density of 200 times the critical density of the universe.

McGaugh et al. (2009[6]) estimate this ratio in smaller structures, on the scale of galaxies, and report that the baryon content increases with the mass of the halo, but remains far below the mass expected based on cosmological values. The missing baryons could be outside the virial radius, either because they have never fallen into the halo, or because they were ejected. Of the gas that remains within the virial radius, a significant portion lies within the galaxy ($r_{gal} = 0.15 \times r_{200}$), and is forming stars. The rest, referred to as the circumgalactic medium (CGM), extends throughout the virial sphere, and can be in many different states, some of which are difficult to observe.

Werk et al. (2014[9]) attempted to model the CGM to determine its mass, using spectra of sightlines towards distant quasi-stellar objects (QSOs), as part of the COS-Halos survey (Werk et al., 2011[32]). These sightlines pass between a projected distance of 5 kpc and 150 kpc from 67 low-redshift galaxies. The authors modeled the column densities of HI gas, and low and intermediate mass metal ions in the intervening galaxies using CLOUDY (Ferland et al., 2013[33]). These lines are sensitive to cool ($T < 10^5 K$) gas, which they refer to as the cool CGM (CCGM). The authors assumed that (i) the low and intermediate ions observed in the COS spectra are a result of a single gas phase with the same origin as the ions, (ii) the lines are only the result of the CCGM, where photoionization dominates, (iii) the absorption from the low and intermediate ions trace the majority of the HI gas, and (iv) that the gas is in ionization equilibrium. Their analysis yields a best fit for the radial dependence of the CCGM density of $r^{-0.8}$, and a mass which accounts for over 30% of the expected baryonic mass of a system of $M_{200} = 1.5 \times 10^{12} M_{\odot}$.

Stern et al. (2016, [34]) revised this model by allowing the CCGM to assume a wide range of densities, between 50 and 5×10^5 times the cosmic mean. This method pushes the estimated cool CGM mass down by a factor of 5, reducing it to 5-6% of the expected baryonic mass, with a radial profile proportional to r^{-1}.

From this previous work it is clear that the CGM is an important reservoir of baryons within a halo, but its spatial distribution and total mass is uncertain. This thesis will address these issues with the APOSTLE simulations (introduced in 1.7). In addition, the inventory of metals throughout the halo will be examined, as well as

the metallicities of the remaining baryons.

2.1.1 Galaxy Selection From Numerical Simulations

In this chapter, I will be using the APOSTLE simulations to perform a comprehensive census of the baryonic content of a wide range of galaxies. The sample considered consists of isolated galaxies made up of APOSTLE centrals and primaries (described in section 1.7) with $M_{200} > 5 \times 10^9 M_\odot$, and $M^* > 10^5 M_\odot$.

2.2 APOSTLE Baryon Fractions

Figure 2.1 shows, as a function of virial mass, the mass of baryons within r_{200}. The green points show the total baryonic mass within the virial radius of the sampled galaxies and is below the mass expected from the cosmological fraction (shown as the dashed line labelled 100%) across the entire range of virial masses. Stellar mass, shown in blue, is well below the total baryonic mass in most cases, which means that a majority of the baryons are in gaseous form.

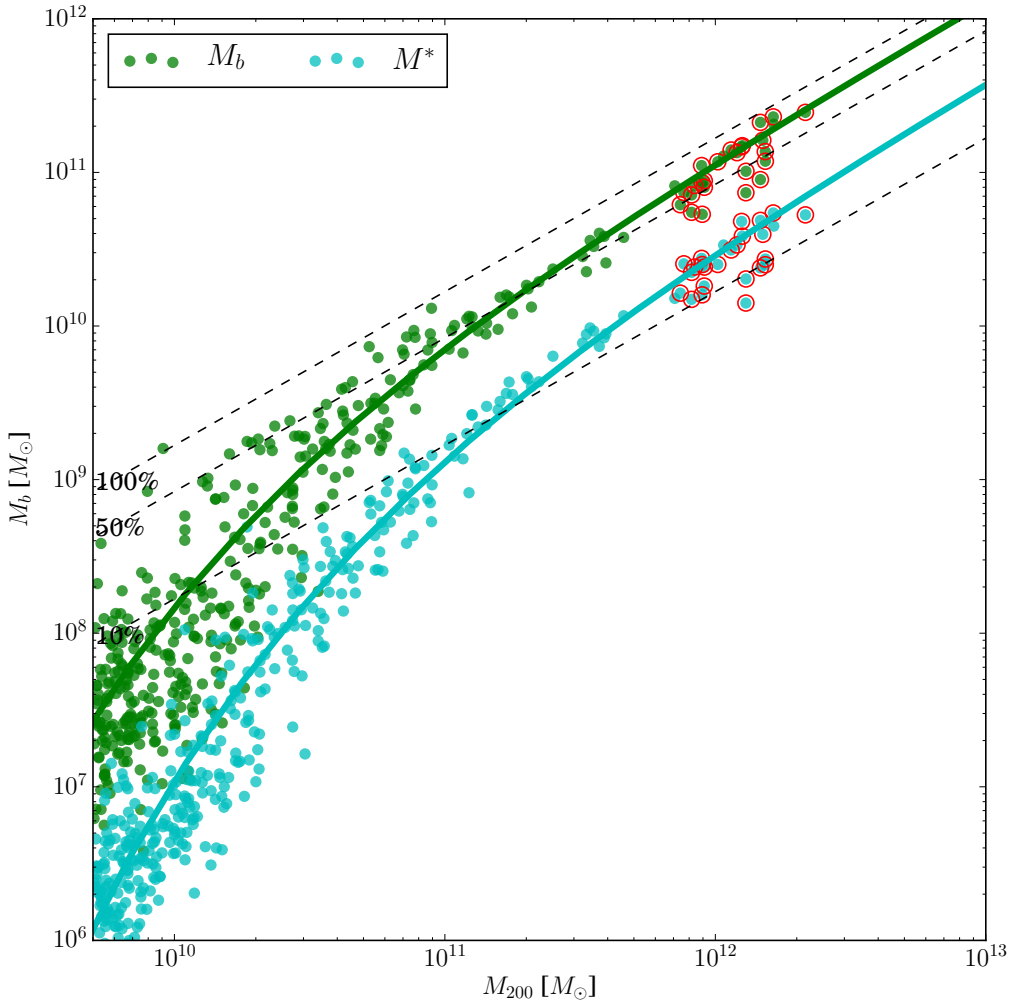

Figure 2.1: Baryonic and stellar mass as a function of virial mass for a wide range of APOSTLE centrals. Primary galaxies are circled in red. The dashed lines correspond to fractions of f_b, and the green and blue lines were fit to the mean masses in 25 bins of M_{200}. The fitting function is $M = A\frac{M_{200}}{M_S}e^{\left(-\frac{M_{200}}{M_S}\right)^{\alpha}}$, and the fit parameters are given in Table 2.1

Figure 2.2 shows that the gas and stars within the virial radius are distributed differently. The stars are very centrally concentrated, and the inner green circle, representing $r_{gal} = 0.15 \times r_{200}$, contains a majority of the stellar mass in the virial radius. We will use this radius to define the central galaxy of a halo. Stars beyond this are seen in the form of smaller satellites, as shown in the top left subplot. These

satellites trace the most massive subhalos from the top right subplot. The gas, on the other hand, does not seem to be confined to the highest mass subhalos, and can extend across the entire virial sphere, as seen in the bottom two subplots.

On average, mass-weighted temperature is quite high, on the order of the virial temperature of the halo. This temperature is given by:

$$T_{vir} = \frac{\mu m_p}{2k_B} \frac{GM_{200}}{r_{200}} \tag{2.1}$$

Where m_p is the proton mass, and μ is a constant based on the primordial mixture of elements. G is the gravitational constant. For APOSTLE galaxies at z=0, this equation becomes:

$$T_{vir} = 35.9 \times 4.302 \times 10^{-6} \frac{M_{200}}{r_{200}} \left(\frac{Kkpc}{M_\odot}\right) \tag{2.2}$$

When examining density, the densest gas traces the most massive dark matter subhalos, which correspond to the primary galaxy, and its massive satellites.

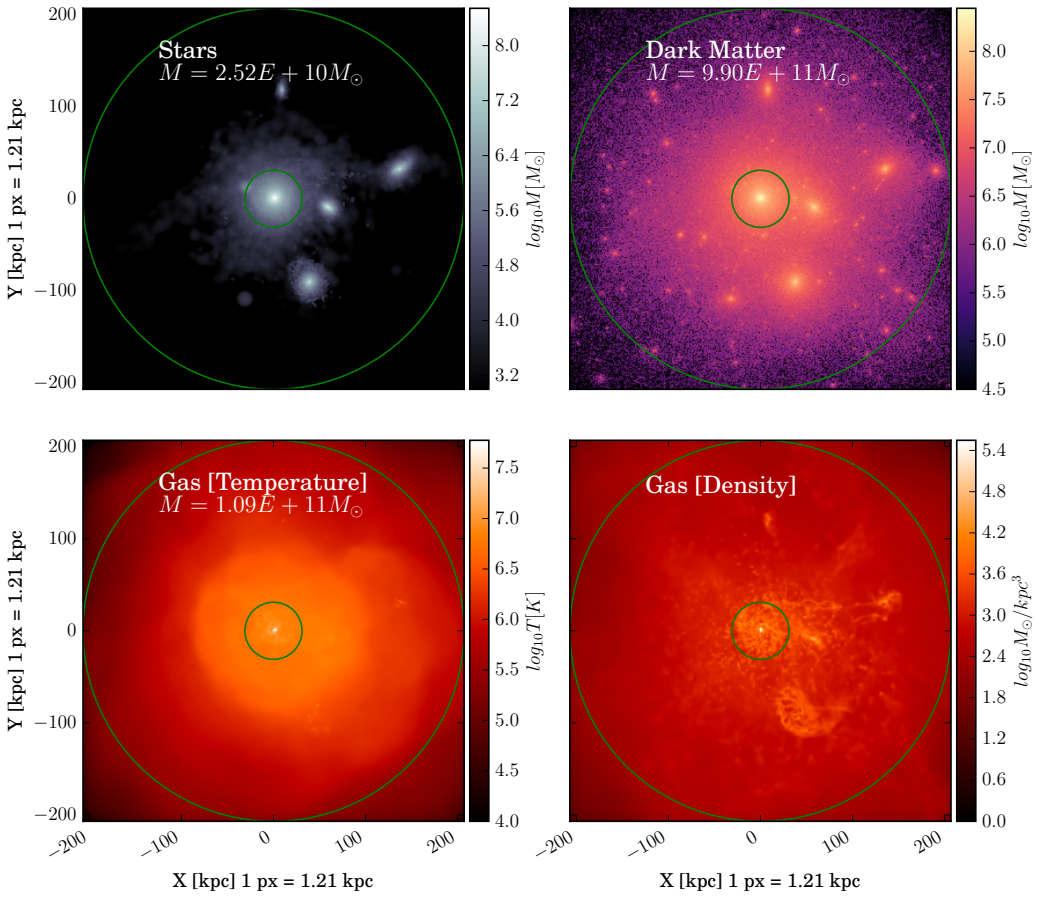

Figure 2.2: Face-on renderings of AP1-L2 G1, in each different form of matter. Green circles indicate the virial radius of the halo. (Top Left) Star particle distribution coloured by line of sight mass. (Top Right) DM particle distribution, coloured by line of sight mass. (Bottom Left) gas particles coloured by mass-weighted temperature. (Bottom Right) gas particles coloured by pixel column density.

The gas is quite complex, and covers a wide range of temperatures and densities, as shown in Figure 2.3. We identify three different regions in this plane. The first is the gas which is forming stars, which is typically at the centres of satellites and galaxies. The rest, which is CGM gas, is split into gas with a temperature below $10^5 K$ (the CCGM), as defined by the COS-Halos observations, and that which is above this

temperature limit (the WHCGM). This distinction is shown by the horizontal blue line. The masses of these categories in this halo (AP1-L2 G1) is given on the figure, as well as the total virial mass, and the total mass in stars.

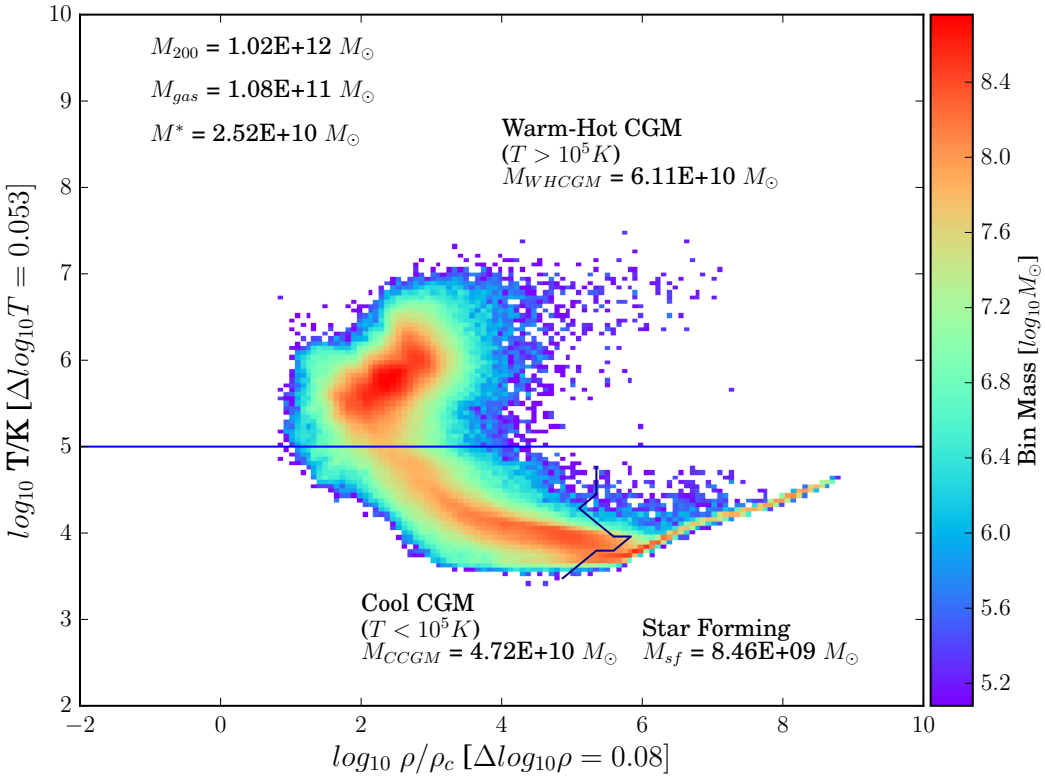

Figure 2.3: Temperature-density diagram for a primary galaxy (AP1-L2 G1) in APOSTLE Volume 1. The $10^5 K$ limit between the CCGM and WHCGM is shown as a blue line, and a smaller line at low temperatures and high densities demarcates the star-forming gas.

Gas at low densities and high temperatures has a long cooling time, which results in a build-up, or high concentration of gas particles at roughly $10^6 K$. This reservoir, which makes up the bulk of the WHCGM, is fed both by infalling material, and by gas blown off the disk by feedback mechanisms. Gas that has been heated recently by feedback, and which has not had time to cool, composes the arm of hot gas extending into the high-density range. These particles are still near the star-forming regions at the centre of the galaxy, but will soon join the WHCGM as they expand outwards into the halo.

As gas cools, it loses pressure support and moves to higher densities and lower temperatures, which explains the shape of the CCGM arm.

The spatial distribution of these categories is quite distinct, as shown in Figure 2.4, where the star-forming gas, WHCGM, and CCGM are rendered separately, for the same simulated galaxy as in Figure 2.2.

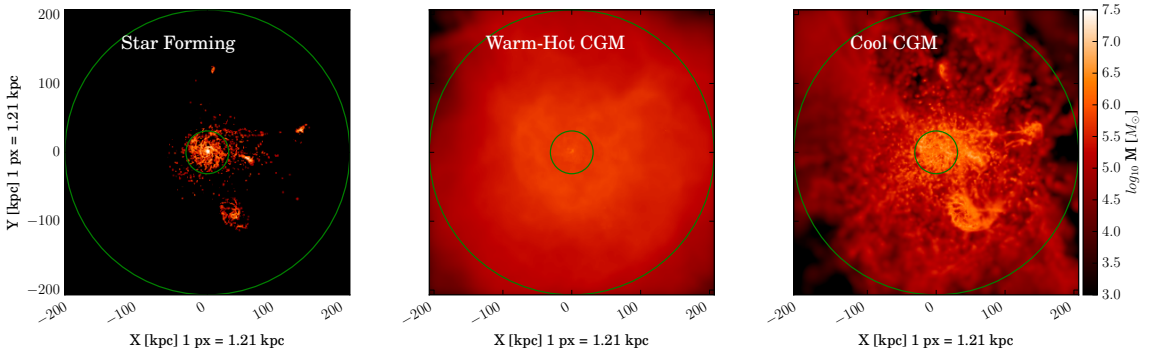

Figure 2.4: Different gas categories in the AP1 L2 Secondary - Left: Star-Forming gas render, Middle: Warm-Hot CGM, Right: Cool CGM. The colours correspond to line of sight sum over a cube with side-lengths equal to the virial radius. Pixel dimensions are given in the axis labels.

The star-forming gas traces the locations of the stars extremely well, and is also confined to the centres of the massive substructures in the halo. Star-forming gas outside of the inner r_{gal} circle is primarily found in massive satellites.

The WHCGM fills the halo entirely, but has almost no substructure. It gives the impression of being in hydrostatic equilibrium. The CCGM is composed of gas that has cooled out of the WHCGM. This gas is clumpy, and in-falling (which will be demonstrated later). This is more pronounced at the centres of the halo and the massive subhalos, where the gas is denser, but this also occurs at large distances from the galaxy.

2.2.1 Radial Profiles

To characterize the differences between the CGM, and its WHCGM and CCGM components, Figure 2.5 displays spherically-averaged radial dependencies of the tem-

perature, density, and radial velocity of this gas. These averages were calculated from the average across all 24 APOSTLE primary galaxies (the M31 and MW analogues), which will be henceforth referred to as the Average Primary (AP). The average virial parameters, and virial temperature calculated with Equation 2.2 are also shown.

The mass-averaged CGM temperature, given by the black points on the uppermost subplot, remains at roughly the virial temperature across the halo, until around 100kpc from the centre of the AP, where it begins to fall. The average CGM density, on the middle subplot, remains high in the innermost 20kpc, with a radial dependence of r^{-1}, and begins to steeply descend as $r^{-5/3}$ for two orders of magnitude to the virial radius. The best-fit parameters for a broken power-law function

$$f(r) = \begin{cases} A(\frac{r}{r_B})^{-\alpha_1} & r < r_B \\ A(\frac{r}{r_B})^{-\alpha_2} & r \geq r_B \end{cases} \tag{2.3}$$

are provided in Table 2.2.

The WHCGM stays above the virial temperature of the halo for the innermost 100 kpc, and dominates the mean temperature. The density is not as centrally concentrated as that of the average CGM, but only decreases proportional to $r^{-0.8}$ out to 150 kpc, where it begins to decrease with r^{-2}. The radial velocity profile shows a large positive spike near the centre of the average APOSTLE primary, which is due to feedback. For the majority of the profile, the WHCGM radial velocity is near-zero.

The CCGM does not dominate the average temperature, but does dictate CGM density for the innermost radii, where it has a radial density dependence proportional to roughly $r^{-0.9}$. This changes 20 kpc from the centre of the average primary galaxy, where the radial dependence becomes r^{-2}. The CCGM radial velocity has the same shape as that of the WHCGM, but is negative over all radii. This infall velocity is roughly constant at 50 km/s.

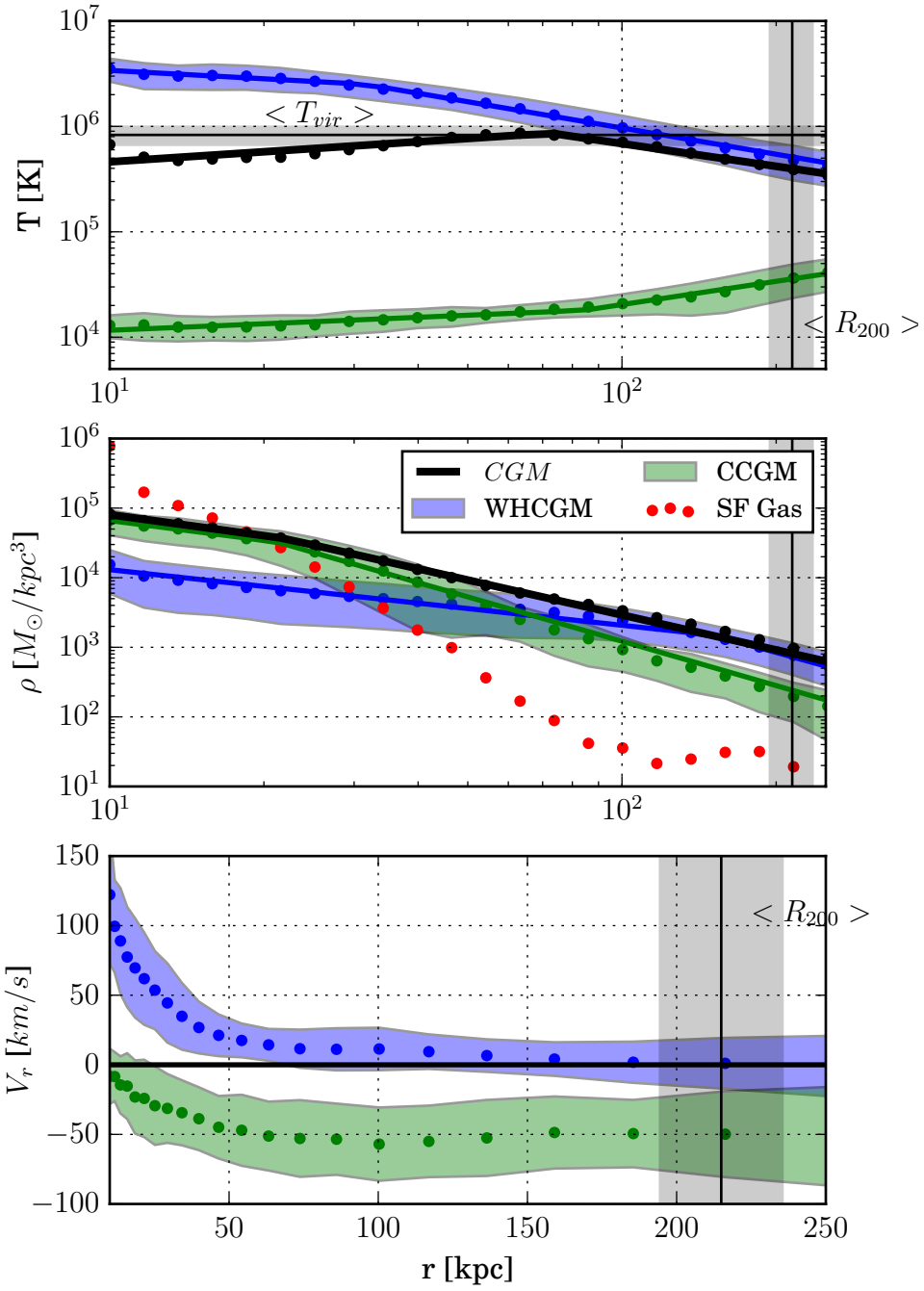

Figure 2.5: The spherically-averaged temperature, density, and radial velocity profiles for the average of all APOSTLE L2 primary galaxies. In the top plot, the horizontal line with bounds is $< T_{vir} > \pm \sigma T_{vir}$. The vertical black line with bounds in all plots is $< r_{200} > \pm \sigma r_{200}$.

The radial density dependence of the COS-Halos CGM is estimated to be $r^{-0.8}$ to

$r^{-1.0}$ (Werk et al.,2014[9] ; Stern et al., 2016[34]), which is consistent with the innermost regions of the average APOSTLE primary. While the COS data has sightlines up to 150 kpc from the centre of each respective galaxy, nearly half (15) of the 33 used in both papers are from within, or near r_{gal}. As is shown in Figure 2.5, within 30 kpc the CCGM is dominant over the WHCGM. The CCGM is not necessarily representative of the CGM as a whole, and only makes up 12% on average of the expected baryonic mass in APOSTLE galaxies, whereas the WHCGM accounts for nearly 30% (from Table 2.3).

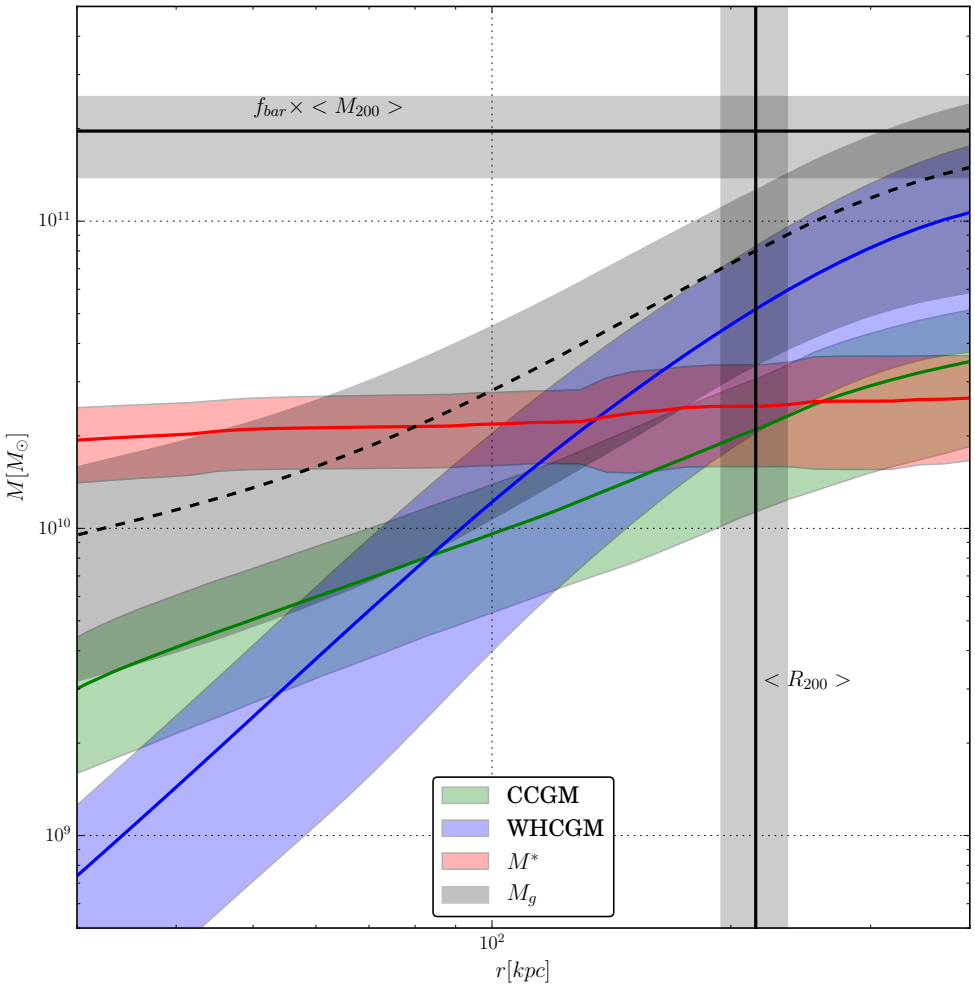

Figure 2.6: Cumulative baryon mass for the averaged APOSTLE primaries and secondaries from 30 kpc to 400 kpc from the centre of the halo. Total gas mass is displayed by a dashed black line, and the mean expected baryon fraction and mean virial radius are shown in solid black horizontal and vertical lines.

Figure 2.6 shows the cumulative mass profiles of stars, WHCGM, CCGM, and total gas in the average primary. The stellar mass profile does not increase by much over the plotted radii because a majority (roughly 80% on average) of the stellar mass lies within the 30 kpc lower bound, within r_{gal}. At the AP virial radius, the WHCGM has a mass of approximately $5 \times 10^{10} M_{\odot}$, with half of that within 150 kpc of the AP centre, where the density profile begins to steeply descend. The CCGM has a mass of $2 \times 10^{10} M_{\odot}$, with 50% contained within 100 kpc. This is comparable to the AP stellar mass within the virial radius.

As shown in Table 2.3, baryonic mass is very unevenly distributed within the halo. For the average APOSTLE L2 primary galaxy, only 60% of the expected cosmological baryonic mass is retained within the virial radius. The APOSTLE primary with the highest retained fraction, AP1-L2 G0, has 84% of its expected baryonic mass within its virial radius, which is well beyond one standard deviation from the average. This galaxy also has nearly half (48%) of its expected baryonic mass in the WHCGM, compared to just 10% in the CCGM. Despite the fact that this galaxy is an outlier, there is a definitive trend towards the WHCGM containing over double the mass of the CCGM. Based on Figure 11 from Werk et al. (2014[9]), even with the re-calculated CCGM mass from Stern et al. (2016[34]), the WHCGM must be on the higher end of the observationally-motivated estimate for its mass range.

2.3 Metals and Metallicity in APOSTLE halos

Metallicities are a crucial component of the baryonic matter in a halo. Metal lines are one of the primary sources of cooling in the range of temperatures between $10^5 K$ and $10^7 K$.

Metals can be traced through absorption lines, as done in Werk et al. (2014[9]), and can be used to determine the best-fitting metallicity and density of the CCGM, but not the WHCGM. This is important because, as shown in the previous section, the WHCGM contains a majority of the baryonic mass in APOSTLE galaxies.

Metals are produced by stars, and some of those metals are locked in the long-lived stars and stellar remnants; however the rest is released into the CGM. In APOSTLE, as in EAGLE, the total mass ejected from a star particle is determined by the initial

mass function (IMF; Schaye et al., 2015[13]). This IMF, and chosen stellar yields, mean that the total mass of metals produced in the volume is approximately 5.5% of the mass of the long-lived stars.

On the left panel of Figure 2.7, total metal mass within the virial radius is plotted in blue against total stellar mass within the virial radius for all galaxies in the sample in the range $10^6 M_\odot < M^* < 10^{11} M_\odot$. This has been fit by a broken power-law function shown in black. The masses of metals held in the stars within the virial radius are shown by the red points, which have been fit with the red broken power-law function. The 5.5% expectation is shown as a dashed line. At masses below $9.5 \times 10^8 M_\odot$, the power-law slope of the total metal mass is nearly unity, which means that past a certain minimum mass, the fraction of metals retained is independent of stellar mass.

The right panel splits the total metal mass held in the gas between star-forming gas (cyan), and CGM gas (black). At masses below $10^9 M_\odot$, a majority of the metals are held in the CGM. At $M^* > 10^9 M_\odot$, the mass of metals held in the stars is equal to that held in the CGM.

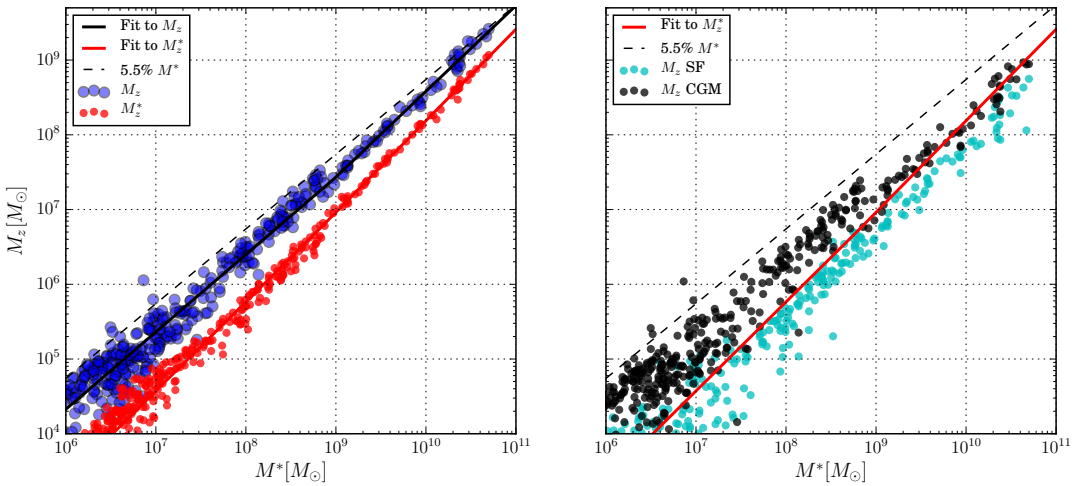

Figure 2.7: The stellar-mass dependence of the metal mass held in various forms of matter. On the left panel, blue points correspond to the total metal mass, and red to the mass of metals held in the stars. On the right panel, the black points display the mass of metals in the CGM gas, and the cyan show the mass of metals in the star-forming gas. The fit to the total metal mass is shown with a black line, and the fit to the stellar metal mass is shown with a red line. The fits have the same form of broken power law as in Figure 2.5, with parameters $A = 2.59 \times 10^7 M_\odot$, $M_S = 9.58 \times 10^8 M_\odot$, $\alpha_1 = -1.03$, and $\alpha_2 = -1.15$. The fit to the stellar metal mass has the parameters $A = 4.89 \times 10^6 M_\odot$, $M_S = 5.97 \times 10^8 M_\odot$, $\alpha_1 = -1.19$, and $\alpha_2 = -1.22$.

In Figure 2.8 we show the metal mass held in the two CGM categories. For galaxies that are below $10^9 M_\odot$ in stellar mass, the distinction between WHCGM and CCGM is not meaningful, because the temperature of the WHCGM becomes comparable to the $10^5 K$ distinction from the CCGM.

We find that in large galaxies, the mass of metals held in the WHCGM is comparable to that held in the CCGM. In smaller galaxies, the CCGM holds more. As shown in Table 2.3 for the APOSTLE primaries, the WHCGM in large galaxies has over twice the baryonic mass of the CCGM, which means that in these massive galaxies, the concentration of metals in the CCGM should be twice that of the WHCGM.

The right panel of Figure 2.8 shows the metallicity of each baryon component in units of solar metallicity. The stellar metallicity-stellar mass relation from the EAGLE simulations (de Rossi et al., 2017[35]) is provided for comparison by the dashed line, with 25th and 75th percentile bounds. The total metal masses in each compo-

nent for the APOSTLE primary galaxies is given in Table 2.4.

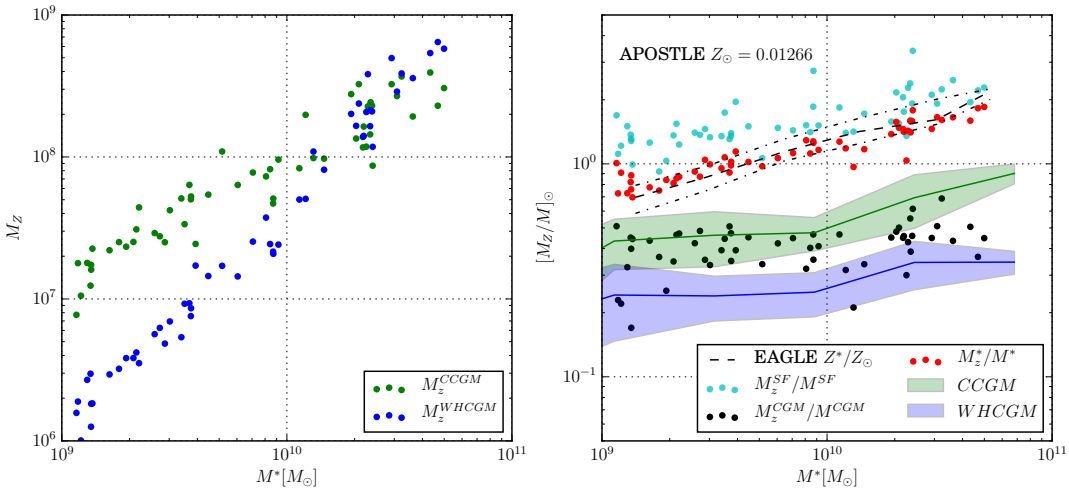

Figure 2.8: Left: The metal masses held in the WHCGM (blue) and CCGM (green) as functions of stellar mass. APOSTLE primaries are circled in red. Right: Baryon metallicities in solar units, with EAGLE M_z^*/M^* for comparison.

The fact that the stars contain a majority of the metal mass within a halo helps to explain why the metal retention fraction does not steeply descend with stellar mass. Stars, as seen in Figure 2.2, are concentrated within r_{gal}, and are thus tightly bound to the halo. The CGM gas that is most likely to escape does not have high metallicity. This means that its loss will have a negligible effect on the total metal mass within a halo.

Figure 2.8 suggests that the gas which has cooled out of the WHCGM to form the CCGM has been able to do so partially due to its higher metallicity. The difference in radial distribution of the two components, as shown in Figure 2.6, means that the CGM metallicity can vary widely depending on where it is sampled, as well as whether the chosen ionic lines correspond to the WHCGM or the CCGM.

2.4 Summary

Our analysis of the baryonic and metal retention of isolated galaxies in the APOSTLE simulations leads us to the following conclusions:

- **The categories of baryonic mass, and the CGM:** Baryons within the virial bounds of a halo can take the form of stars, star-forming gas, or CGM gas. The CGM gas in massive galaxies ($M^* > 10^9 M_\odot$) can be separated into a WHCGM ($T > 10^5 K$), and a CCGM ($T < 10^5 K$). The WHCGM is virialized, and has a shallow mass density profile. The CCGM, which is the gas sampled by the ionic lines in the COS sample (Werk et al., 2012[32]), is clumpy and in-falling, and has a steeper density profile proportional to r^{-2}.

- **Average ejection of baryons from primary galaxies:** For APOSTLE primary galaxies at redshift zero, approximately 40% of the mass of baryons expected based on the cosmological fraction have been ejected, or prevented from falling into the virial radii of their dark matter halos.

- **The retention of baryonic mass in primary galaxies, by category:** Of the expected baryon mass for the APOSTLE primary galaxies, on average 59%$\pm$ 15% is retained within the virial radius. $15\% \pm 4\%$ is retained as stars, $4\% \pm 2\%$ as star-forming gas, $29\% \pm 9\%$ in the WHCGM, and $12\% \pm 5\%$ in the CCGM.

- **Average ejection of metals from primary galaxies:** For APOSTLE primary galaxies at redshift zero, approximately 30% of the expected mass of metals have been lost.

- **The retention of metal mass in primary galaxies, by category:** Of the expected metal mass for the APOSTLE primary galaxies, on average $69\% \pm 10\%$ is retained within the virial radius. $31\% \pm 5\%$ is held in stars, $12\% \pm 4\%$ in star-forming gas, $14\% \pm 4\%$ in the WHCGM, and $13\% \pm 4\%$ in the CCGM.

- **Comparison between baryon retention and metal retention:** The retained fraction of metals is higher, but comparable to the retained fraction of baryons. This means that the metals were ejected from the halo in lower-metallicity CGM gas.

- **Comparison of metallicity in the CGM categories:** The CCGM has a higher metallicity than the WHCGM, most likely because cooling is faster for metal-enriched gas.

2.5 Tables

Table 2.1: Parameters for the best fit lines in Figure 2.1.

	$log_{10}A/M_\odot$	$log_{10}M_S/M_\odot$	α
M_b	9.779	10.649	-0.533
M^*	9.758	11.136	-0.495

Table 2.2: Table of broken power law parameters for the WHCGM, CCGM, and mass-averaged total, as shown in Figure 2.5.

	A	r_B	α_1	α_2
T_{WHCGM}	2.51×10^6K	31.54 kpc	0.26	0.83
ρ_{WHCGM}	1.49×10^3 $M_\odot/kpc^3$	151.09 kpc	0.80	2.03
T_{CCGM}	1.80×10^4K	84.24 kpc	-0.20	-0.73
ρ_{CCGM}	2.98×10^4 $M_\odot/kpc^3$	20.29 kpc	0.91	1.98
T_{CGM}	8.6×10^5K	72.46 kpc	0.94	2.12
ρ_{CGM}	3.66×10^4 $M_\odot/kpc^3$	21.93 kpc	1.00	1.67

Table 2.3: Table of the breakdown of baryons retained within the virial radius of the primary APOSTLE galaxies. The average is given in the last row. Fractions of the expected total are provided in brackets.

Galaxy ID	$log_{10}\ M_{200}/M_\odot$	$log_{10}\ f_b \times M_{200}/M_\odot$	$log_{10}\ M^*/M_\odot$	$log_{10}\ M_{WHCGM}/M_\odot$	$log_{10}\ M_{CCGM}/M_\odot$	$log_{10}\ M_{SFGas}/M_\odot$	$log_{10}\ M_b/M_\odot$
AP1-L2 G0	12.214	11.438	10.736(0.199)	11.117(0.478)	10.400(0.092)	10.288(0.071)	11.361(0.839)
AP1-L2 G1	12.009	11.232	10.401(0.147)	10.681(0.281)	10.553(0.209)	9.927(0.050)	11.069(0.687)
AP2-L2 G0	11.871	11.094	10.214(0.132)	10.461(0.233)	10.108(0.103)	9.542(0.028)	10.790(0.496)
AP2-L2 G1	11.884	11.107	10.405(0.199)	10.484(0.238)	10.133(0.106)	9.657(0.035)	10.869(0.578)
AP3-L2 G0	12.175	11.399	10.597(0.158)	10.946(0.353)	10.377(0.095)	9.996(0.040)	11.209(0.645)
AP3-L2 G1	12.080	11.304	10.528(0.168)	10.710(0.255)	10.573(0.186)	10.077(0.059)	11.128(0.668)
AP4-L2 G0	12.100	11.323	10.585(0.183)	10.919(0.394)	10.239(0.082)	10.026(0.050)	11.174(0.710)
AP4-L2 G1	12.097	11.321	10.681(0.229)	10.768(0.280)	10.453(0.136)	10.076(0.057)	11.167(0.702)
AP5-L2 G0	11.949	11.173	10.440(0.185)	10.645(0.297)	10.498(0.212)	9.879(0.051)	11.045(0.744)
AP5-L2 G1	11.923	11.147	10.384(0.173)	10.491(0.221)	10.332(0.153)	9.744(0.040)	10.915(0.586)
AP6-L2 G0	12.333	11.557	10.724(0.147)	11.229(0.470)	10.292(0.054)	9.612(0.011)	11.391(0.683)
AP6-L2 G1	12.059	11.282	10.495(0.163)	10.799(0.329)	10.481(0.158)	10.190(0.081)	11.146(0.731)
AP7-L2 G0	12.113	11.337	10.306(0.093)	10.726(0.245)	10.386(0.112)	9.594(0.018)	11.007(0.468)
AP7-L2 G1	12.113	11.336	10.150(0.065)	10.456(0.132)	10.412(0.119)	9.633(0.020)	10.862(0.336)
AP8-L2 G0	12.185	11.408	10.436(0.107)	10.847(0.274)	10.188(0.060)	9.718(0.020)	11.073(0.462)
AP8-L2 G1	12.185	11.408	10.399(0.098)	10.828(0.263)	10.542(0.136)	9.963(0.036)	11.135(0.533)
AP9-L2 G0	11.912	11.136	10.349(0.163)	10.523(0.244)	10.061(0.084)	9.620(0.030)	10.853(0.522)
AP9-L2 G1	11.912	11.136	10.174(0.109)	10.364(0.169)	10.104(0.093)	9.618(0.030)	10.740(0.402)
AP10-L2 G0	12.167	11.390	10.688(0.198)	11.008(0.414)	10.641(0.178)	10.241(0.071)	11.326(0.862)
AP10-L2 G1	12.167	11.390	10.378(0.097)	10.576(0.153)	10.317(0.084)	9.868(0.030)	10.953(0.365)
AP11-L2 G0	11.959	11.183	10.384(0.159)	10.583(0.251)	10.048(0.073)	9.805(0.042)	10.903(0.525)
AP11-L2 G1	11.959	11.182	10.260(0.120)	10.589(0.255)	10.408(0.168)	9.764(0.038)	10.946(0.580)
AP12-L2 G0	11.952	11.175	10.400(0.168)	10.307(0.135)	9.775(0.040)	9.300(0.013)	10.727(0.356)
AP12-L2 G1	11.951	11.175	10.203(0.107)	10.475(0.199)	10.517(0.220)	9.838(0.046)	10.932(0.572)
Average	12.071 ±0.300	11.294 ±0.300	10.463(0.148) ±0.414(0.042)	10.756(0.290) ±0.635(0.094)	10.369(0.119) ±0.416(0.052)	9.890(0.040) ±0.580(0.018)	11.070(0.597) ±0.455(0.146)

Table 2.4: Table of the breakdown of metals retained within the virial radius of the primary APOSTLE galaxies. The average is given in the last row. Fractions of the expected total are provided in brackets.

Galaxy ID	$log_{10}\ M^*/M_\odot$	$log_{10}\ f_z \times M^*/M_\odot$	$log_{10}\ M_z^*/M_\odot$	$log_{10}\ M_z^{WHCGM}/M_\odot$	$log_{10}\ M_z^{CCGM}/M_\odot$	$log_{10}\ M_z^{SFGas}/M_\odot$	$log_{10}\ M_z/M_\odot$
AP1-L2 G0	10.736	9.476	9.083(0.405)	8.763(0.193)	8.485(0.102)	8.748(0.187)	9.424(0.887)
AP1-L2 G1	10.401	9.141	8.597(0.286)	8.303(0.145)	8.443(0.200)	8.228(0.122)	9.018(0.754)
AP2-L2 G0	10.214	8.955	8.366(0.258)	7.910(0.090)	7.988(0.108)	7.880(0.084)	8.687(0.541)
AP2-L2 G1	10.405	9.145	8.684(0.346)	8.217(0.118)	8.159(0.103)	8.137(0.098)	8.968(0.665)
AP3-L2 G0	10.597	9.337	8.833(0.313)	8.582(0.176)	8.356(0.104)	8.456(0.131)	9.197(0.724)
AP3-L2 G1	10.528	9.268	8.730(0.290)	8.376(0.128)	8.513(0.176)	8.370(0.126)	9.125(0.720)
AP4-L2 G0	10.585	9.325	8.891(0.368)	8.555(0.170)	8.285(0.091)	8.521(0.157)	9.220(0.785)
AP4-L2 G1	10.681	9.421	8.955(0.341)	8.588(0.147)	8.567(0.140)	8.528(0.128)	9.300(0.756)
AP5-L2 G0	10.440	9.181	8.714(0.341)	8.321(0.138)	8.362(0.152)	8.264(0.121)	9.057(0.752)
AP5-L2 G1	10.384	9.124	8.616(0.310)	8.148(0.106)	8.214(0.123)	8.091(0.093)	8.925(0.631)
AP6-L2 G0	10.724	9.464	9.053(0.389)	8.809(0.222)	8.361(0.079)	8.059(0.039)	9.326(0.728)
AP6-L2 G1	10.495	9.235	8.717(0.303)	8.329(0.124)	8.385(0.141)	8.498(0.183)	9.111(0.752)
AP7-L2 G0	10.306	9.047	8.375(0.213)	8.038(0.098)	7.992(0.088)	7.848(0.063)	8.712(0.463)
AP7-L2 G1	10.150	8.890	8.307(0.261)	7.895(0.101)	8.149(0.181)	7.925(0.108)	8.704(0.652)
AP8-L2 G0	10.436	9.176	8.528(0.224)	8.317(0.138)	8.073(0.079)	7.952(0.060)	8.876(0.501)
AP8-L2 G1	10.399	9.139	8.547(0.256)	8.280(0.138)	8.389(0.178)	8.226(0.122)	8.981(0.694)
AP9-L2 G0	10.349	9.090	8.609(0.331)	8.141(0.113)	8.067(0.095)	8.035(0.088)	8.887(0.627)
AP9-L2 G1	10.174	8.914	8.361(0.280)	7.940(0.106)	8.030(0.131)	7.997(0.121)	8.719(0.638)
AP10-L2 G0	10.688	9.428	8.964(0.343)	8.732(0.201)	8.595(0.147)	8.633(0.160)	9.358(0.852)
AP10-L2 G1	10.378	9.119	8.591(0.297)	8.275(0.143)	8.203(0.121)	8.238(0.132)	8.960(0.693)
AP11-L2 G0	10.384	9.124	8.657(0.341)	8.219(0.125)	8.130(0.101)	8.243(0.132)	8.968(0.699)
AP11-L2 G1	10.260	9.000	8.457(0.286)	8.140(0.138)	8.159(0.144)	8.121(0.132)	8.845(0.699)
AP12-L2 G0	10.400	9.140	8.742(0.400)	8.070(0.085)	7.939(0.063)	7.933(0.062)	8.925(0.610)
AP12-L2 G1	10.203	8.943	8.333(0.245)	8.000(0.114)	8.254(0.204)	8.146(0.160)	8.803(0.723)
Average	10.463 ±0.414	9.203 ±0.413	8.713(0.310) ±0.552(0.053)	8.373(0.136) ±0.686(0.035)	8.295(0.127) ±0.447(0.040)	8.285(0.117) ±0.647(0.038)	9.057(0.689) ±0.533(0.099)

Chapter 3

Anisotropies in the Spatial Distribution of Local Group Field Galaxies

The distribution of dwarf galaxies in the Local Group has long been known to be anisotropic. I quantify both the ellipticity and orientation of this spatial distribution using the principal axes of the inertia tensor of the positions of these galaxies. The Zone of Avoidance has little impact on this result, and the short axis is aligned with that of the Supergalactic Plane, and is perpendicular to the vector separating the Milky Way and Andromeda galaxies. APOSTLE local group analogues are found to be similarly anisotropic, and like in the observed Local Group, the minor axis of that distribution is found to be perpendicular to the vector separating the two primaries. The angular momentum of the stellar disk shows weak alignment with the minor axis of the field galaxy distribution. In addition the simulations also suggest that the angular momenta of the two primary dark-matter halos tend to be anti-aligned. Additionally, stellar disks tend to orient themselves in the same direction as their halo.

3.1 Introduction

3.1.1 The Supergalactic Plane

The galaxies surrounding the Local Group out to tens of Mpc from the Milky Way lie preferentially on a planar structure, the Supergalactic Plane (SGP), which is approximately perpendicular to the Milky Way's disk (de Vaucouleurs, 1953[36]). Indeed, the Supergalactic Pole lies very close to the plane of the disk, at $(l, \beta) = (47°, 6°)$, where l and β are the galactocentric longitude and latitude respectively.

3.1.2 The Local Group Plane

In the Local Group, the distribution of galaxies is anisotropic. Previous work has attempted to find alignments between this distribution and the SGP. According to Hartwick (2000[37]), who studied the positions of 13 isolated LG field dwarfs [1], their positions are well-approximated by a flattened ellipsoid with a minor axis in the direction of that of the SGP. Similarly, Pawlowski et al. (2013[38]), when fitting a plane to the field galaxies[2], found that the normal to the plane also points to the short axis of the SGP.

The aim of this chapter is to reanalyze these claims with a larger sample of data, and with more distances, to determine whether the distribution of matter in the local universe has an impact on the distribution of field galaxies in our Local Group, the distribution of the major pair, and galactic rotations.

3.1.3 Galaxy Sample Selection

The sample of Local Group galaxies used in this analysis comes from the Extragalactic Distance Database (Tully et al., 2009[17]). They were selected to be within 3 Mpc of the Milky Way, with a stellar mass of $M^* > 10^5 M_\odot$, calculated from the V or B band magnitudes (depending on the data available for each galaxy) assuming a solar mass-to-light ratio of $M_\odot/L_\odot^{V,B}$.

3.2 Results and Analysis

3.2.1 The Distribution of Local Group Field Dwarf Galaxies

Figure 3.1 shows the positions on the sky of the Local Group galaxies in galactocentric coordinates. Satellites of the MW are coloured black, satellites of M31 are in blue. The remainder, which we define as LG field dwarfs, are in green.

The LG Field Dwarfs appear to avoid the plane of the Milky Way, and are concentrated at the North and South galactic poles. This is shown in Figure 3.2, where

[1] WLM, NGC 55, IC 1613, Leo A, NGC 3109, GR 8, the Sagittarius dwarf irregular, NGC 6822, DDO 210, IC 5152, Tucana, UKS 2323-326, and Pegasus

[2] Local Group field dwarfs/galaxies are defined as those galaxies with a stellar mass greater than $10^5 M_\odot$ within 3Mpc from the Milky Way, that are also further than 300kpc from both of the two primary galaxies. Satellites of the Milky Way or M31 are defined as galaxies within 300kpc of either galaxy, respectively.

we show the distribution in galactic latitude of all LG field dwarfs in bins of equal $|sin\beta|$. We would expect a uniform distribution on the sky to be flat. High $|\beta|$ values are indeed more common, and highlight the anisotropy of the field dwarf distribution.

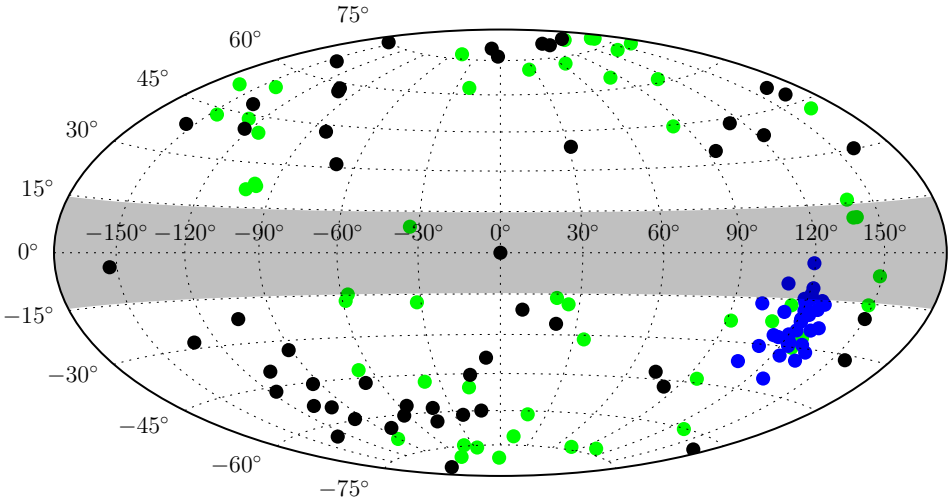

Figure 3.1: Observed LG galaxies with $M^* > 10^5 M_\odot$. Points in blue are M31 satellites, points in black are MW satellites. Green are field galaxies.

The shaded region in Figure 3.1, representing the Zone of Avoidance (Kraan-Korteweg and Lahav, 2000[39]), is marked by the shaded region in Figure 3.2, and takes up approximately 25% of the area of the sky around the galactic disk. We test whether the marked lack of galaxies observed within this latitude range (shown in Figure 3.2), can be explained solely by the Zone of Avoidance. We do this by performing a KS test over the distribution of galaxies between $|\beta| > 14°$, with a null hypothesis of the sample having been drawn from a uniform distribution. The P value returned is 0.002, which allows us to reject that hypothesis at 99.8%. This is in agreement with previous studies which have concluded that the LG field dwarfs are

anisotropic.

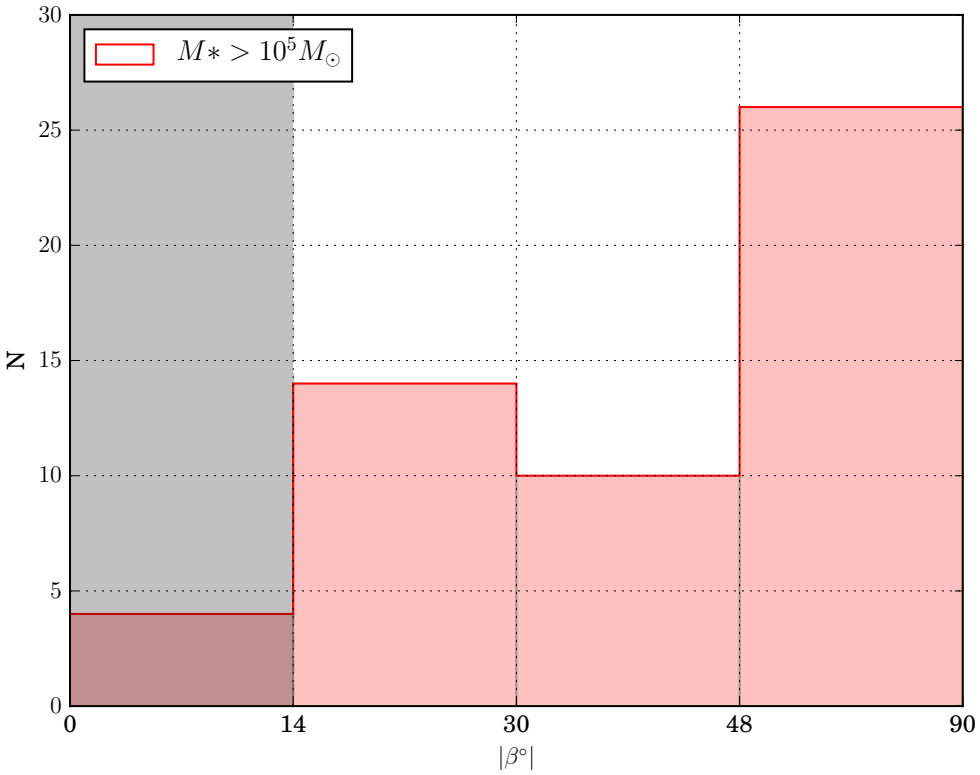

Figure 3.2: A histogram of galactocentric latitude in bins of equal area on the sky. Clearly, this is ill-fit by a uniform distribution of galaxies on the sky, and a lack of galaxies between 0° and 14° is noticeable.

3.2.2 Estimating Anisotropy and the Principal Axes of the Local Group Field Dwarf Distribution

The inertia tensor of LG field dwarf galactocentric coordinates was used recover the ellipticity and principal axes of the galaxy distribution. The ith row and jth column of the unnormalized inertia tensor is defined as:

$$\mathbf{I}_{ij} = \sum_{n}^{N} \vec{x}_{n,i} \times \vec{x}_{n,j} \tag{3.1}$$

where $\mathbf{I}_{ij}$ is the value of the tensor matrix at row i and column j. N is the total number of coordinates to use in the calculation, and $\vec{x}_{n,i}$ is the ith index of the nth coordinate,

centred on the Milky Way. The resulting matrix can then be diagonalized, yielding eigenvectors and eigenvalues.[3] The eigenvalue-sorted ($a^2 > b^2 > c^2$) eigenvectors correspond to the principal axes of the distribution in the coordinate system used to calculate the tensor, and the square root of the ratio of the eigenvalues describes the ellipticity of the distribution. A distribution with a high $\frac{b}{a}$ and a low $\frac{c}{b}$ will be oblate, whereas a high $\frac{c}{b}$ and a low $\frac{b}{a}$ is prolate.

By taking the average of the outer bins from Figure 3.2, for a uniformly distributed histogram, we would expect 16 galaxies in each latitude bin. Under the assumptions of a worst-case scenario for the LG Field Dwarf anisotropy, where the true number of galaxies in the lowest latitude bin is equal to the average of the higher-latitude bins, we are missing 12 galaxies from the $|\beta| < 14°$ zone. In order to test how important this deficit could be, I supplement our sample with up to 12 additional galaxies in the stellar mass range corresponding to our sample, with $|sin\beta| < 0.25$, $0 \leq l < 2\pi$, and a radial distribution matching that of the observed LG field dwarfs.

[3] An eigenvector of a transformation is a non-zero vector which changes by only a scale factor when multiplied by the tranformation matrix. A canonical example is $\hat{H}\vec{\psi} = E\vec{\psi}$, where $\hat{H}$ is the transformation matrix, $\vec{\psi}$ is the eigenvector, and E, the scale factor, is called the eigenvalue.

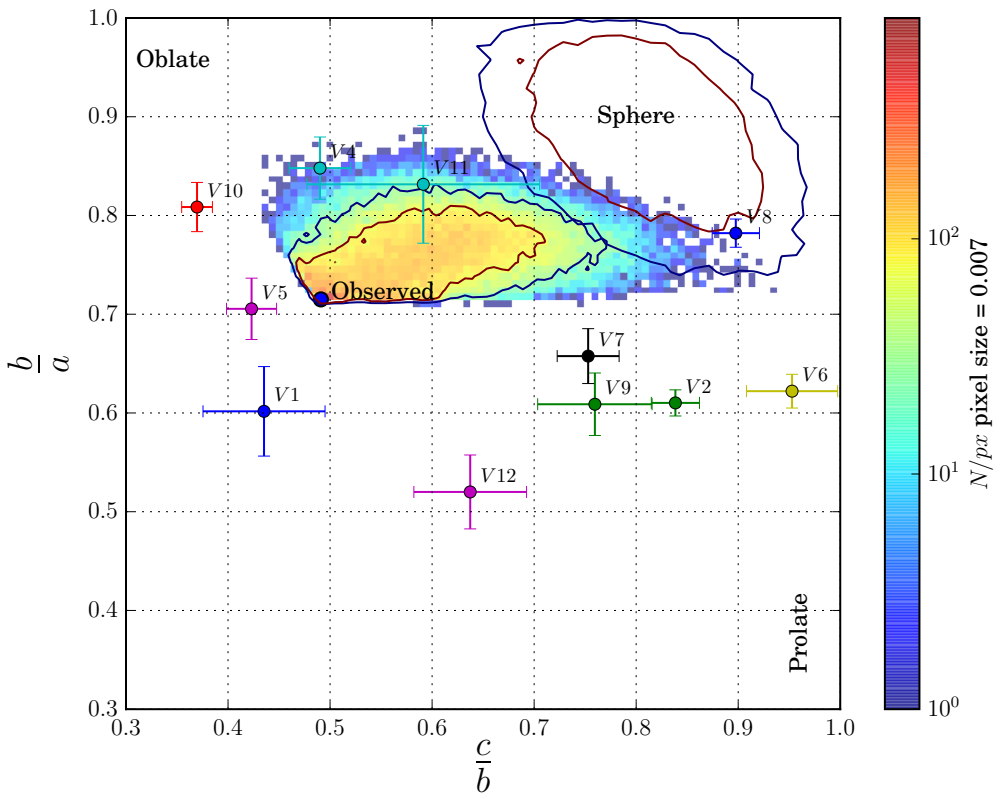

Figure 3.3: The results of a Monte-Carlo exploration of the impact of adding galaxies into the zone of avoidance. The degrees of freedom are the l, β, and r coordinates, as well as the total number of extra galaxies added to the region on the sky close to the galactic disk (N_{added}). The axis ratios for a spherical distribution of the same mean number are plotted as the contours in the upper-right corner, and those for the Local Group as-observed are the blue labelled point.

Figure 3.3 shows the distribution of the eigenvalue ratios over 50,000 realizations of this extended LG field dwarf sample. Red and yellow correspond to more numerous visits to this value, and 1σ and 90% contours are overlaid on the heatmap. The 1σ and 90% contours in the upper right of the plot correspond to a sample of the same mean number where l and $sin\beta$ have been randomized so as to mimic a spherical distribution of the same radial distribution.

The axis ratios for the observed LG field dwarfs is $\frac{c}{b} = 0.49$ and $\frac{b}{a} = 0.72$. The extension of the sample results in a slightly more spherical distribution, as demonstrated in Figure 3.3; however only 3% of the extended samples overlapped with the

spherical distribution of samples. This provides further evidence that the LG Field Dwarfs are distributed anisotropically, even when accounting for a large number of potentially unobserved galaxies within the Zone of Avoidance.

The APOSTLE volumes have a diversity of field dwarf distributions. Some are oblate, some are prolate, but only one has a near-spherical distribution. Nearly all of the simulated local groups are at least as anisotropic as what we observe, however several of the simulation volumes lie within the distribution of extended samples, and the bootstrap error bars of AP11-L2 fall into the 1σ contours.

3.2.3 The Principal Axes of the Local Group Field Galaxy Distribution

We will now examine the directions of the principal axes of the Local Group Field Dwarfs. Figure 3.4 is a Hammer projection in galactic coordinates equivalent to Figure 3.1. Only the field galaxies, shown as green dots, are plotted. Additionally, the position of M31 is shown by a blue diamond. The SGP is overlaid as a thick black line, with North and South Poles displayed as blue stars.

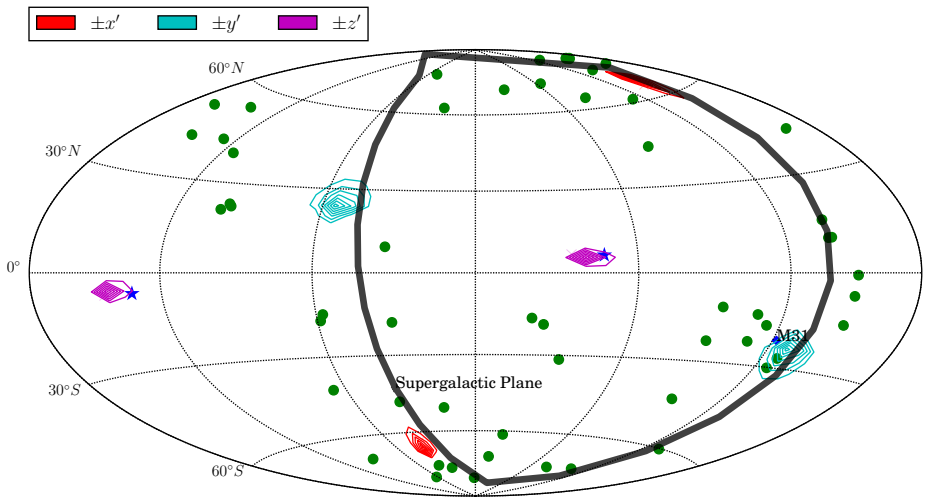

Figure 3.4: Observed LG Field Galaxies in green, with the overlaid SGP shown by a black great-circle. The principal axes of the extended samples are shown by the coloured contours. M31 is shown on the sky as a blue diamond, and the Poles of the SGP are shown by blue stars.

The coloured contours around each principal axis show how their directions change when galaxies are added to the Zone of Avoidance in order to assess the effects of the completeness of the sample. The tightness of the distributions shows that this has very little impact on the axes.

Interestingly, the principal axes are nearly coincident with those of the SGP. The short axis of the LG Field Dwarf distribution (at $(l, \beta) = (42.08^\circ \pm 19.50^\circ, 5.27^\circ \pm 1.68^\circ)$) is closely aligned to that of the SGP, given in Section 3.1.1.

A 3D view of this is shown in Figure 3.5. LG Field Dwarfs are shown as green points, while satellites of the Milky Way and Andromeda galaxies are rendered as black and blue points respectively. The arrow denotes the angular momentum vector of the Milky Way, which lies very close to the $x' - y'$ plane. Two ellipses are drawn on the $x' - y'$ and $y' - z'$ planes with ratios of the major and minor axes equal to the ratios of the principal axes eigenvectors.

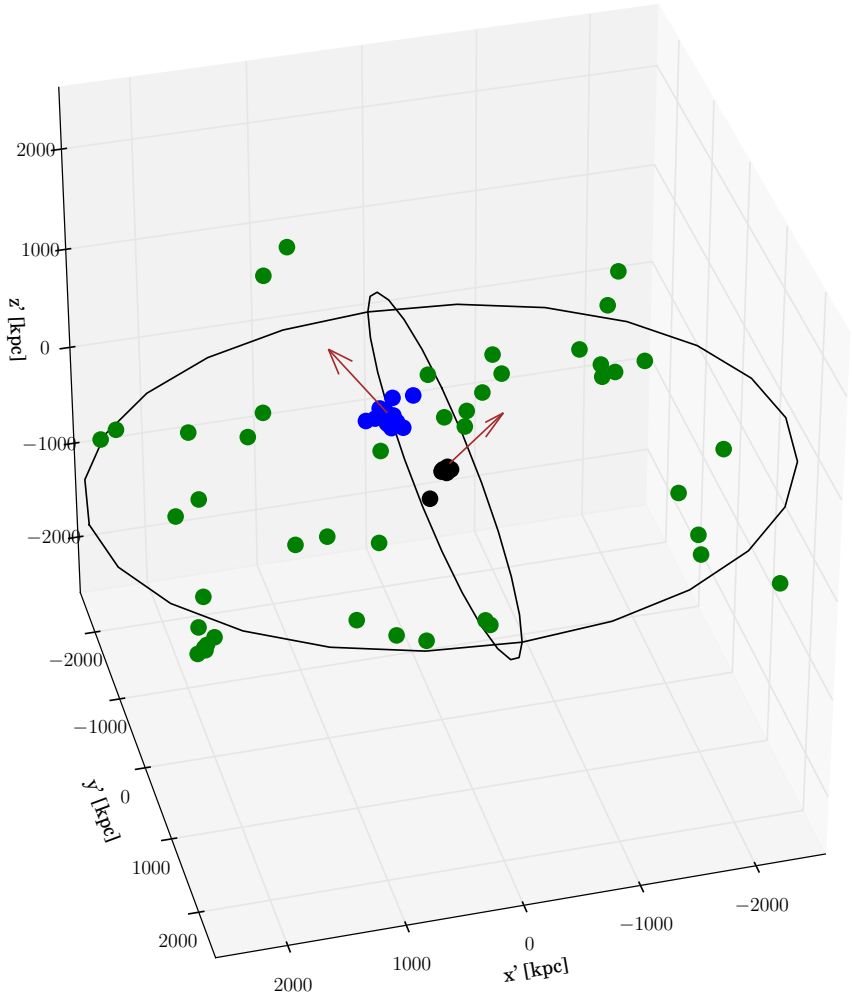

Figure 3.5: Observed LG galaxies oriented with the LG Field Dwarf distribution. Black contours show the axial ratios, and the North Galactic Pole of each primary is shown by an arrow. Satellites of the MW are in black, those of M31 are in blue, and the LG Field Galaxies are in green.

As shown in the earlier Figure 3.4, the $x' - y'$ plane is nearly coincident with the SGP. This means that galaxies which have a small z' coordinate lie close to the SGP. Figure 3.6 shows the distribution of components of the vector that joins the Milky Way and M31 galaxies in the x', y', z' coordinate system over the Local Group realizations. The direction to M31 coincides strongly with the intermediate axis direction in all samples, and the z' fractions are concentrated within 0% to 20%

of the radial distance to M31.

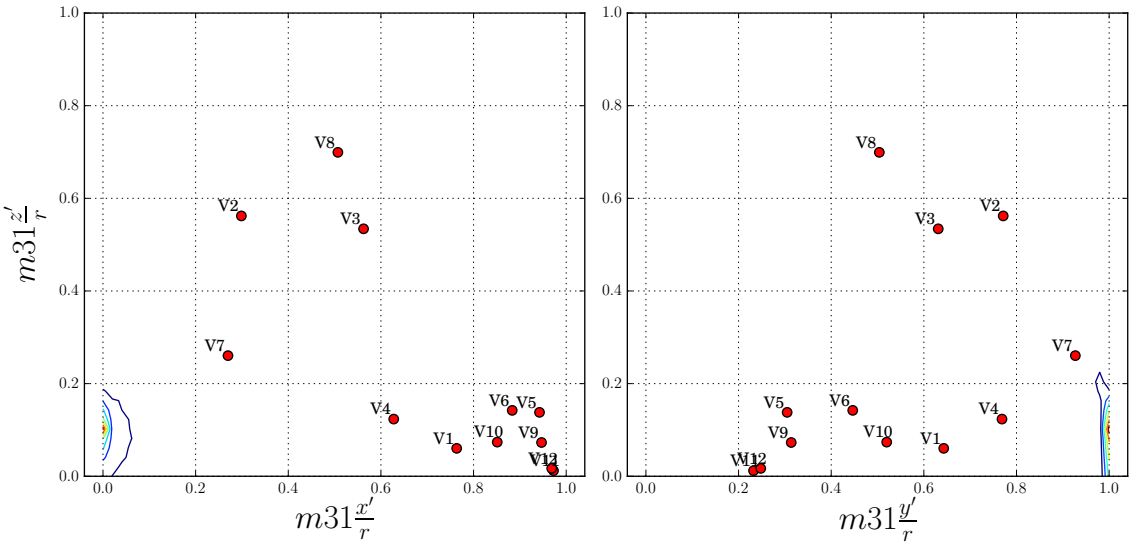

Figure 3.6: M31's $\hat{x}'$ and $\hat{y}'$ components vs. its $\hat{z}'$. The contour shows the distribution of M31 coordinate components for the Local Group realizations. APOSTLE volumes are also shows for comparison.

We check whether this configuration is reproduced in the APOSTLE simulations by also plotting the components of the vector between the two primary galaxies in the Field Galaxy inertia tensor eigenvector basis of each volume as labelled red points. The figure shows that the z' coordinate is much smaller than the x' or y' coordinates, which implies that the vector joining the primaries is also coincident with the $x' - y'$ plane in our simulations. However, unlike the observed Local Group, the simulated M31s appear to be concentrated at the major axis.

3.2.4 Angular Momenta in an Anisotropic Distribution of Matter

As Figure 3.4 shows, the spin of the Milky Way seems to be contained on the $x' - y'$ plane. M31, on the other hand, is inclined at approximately 60° relative to the SGP. We will explore whether there is any correlation between the spins and distribution of matter in the following figures.

Figure 3.7 displays the distribution of APOSTLE primary angular momenta in the reference frame of their field dwarf distributions. The leftmost panel shows the alignment of angular momentum with the major axis. Lower values correspond to

alignment on the $y' - z'$ plane. The middle panel plots alignment along the intermediate axis, and the rightmost panel displays alignment along the minor axis.

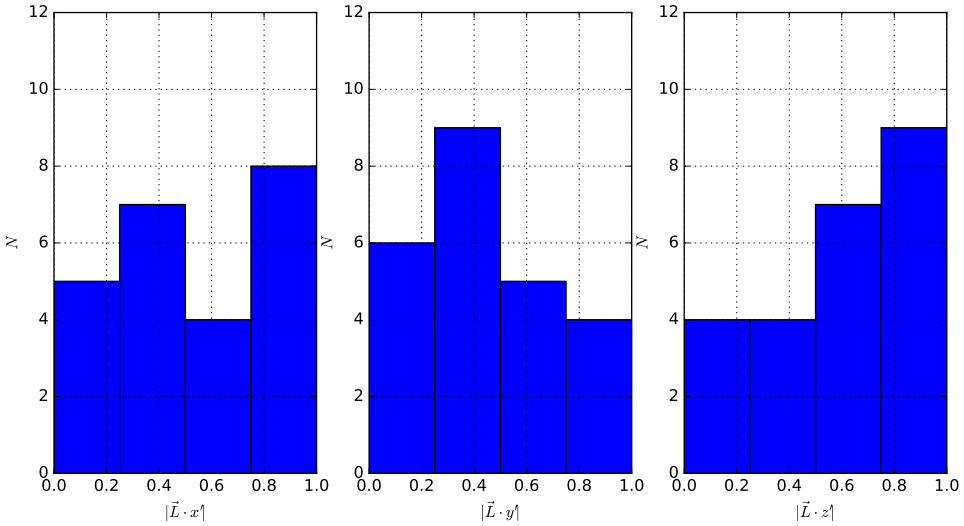

Figure 3.7: Primary and secondary APOSTLE L2 galaxy angular momentum vectors in the field galaxy basis, calculated from the stars within $r_{gal} = 0.15 \times R_{200}$. Each plot shows a histogram of the APOSTLE primary angular momenta dotted with the principal axes of each volume.

The only non-random bias ($P_{KS} = 0.048$) is a weak alignment along z', the minor axis of the field dwarf distribution. M31 is consistent with this result, with a $|\vec{J}_{M31} \cdot z'|$ of 0.83. In contrast, the Milky Way has $|\vec{J}_{MW} \cdot z'|$ of 0.005, and its angular momentum vector lies on the $x' - y'$ plane evenly between the $-x'$ and $-y'$ axes.

Next we explore whether the primary pair orbits in a way that reflects the principal axes and the distribution of matter. Figure 3.8 shows the orbital angular momentum vectors of the 12 APOSTLE primary pairs, in the basis of the principal axes of the field galaxy distribution.

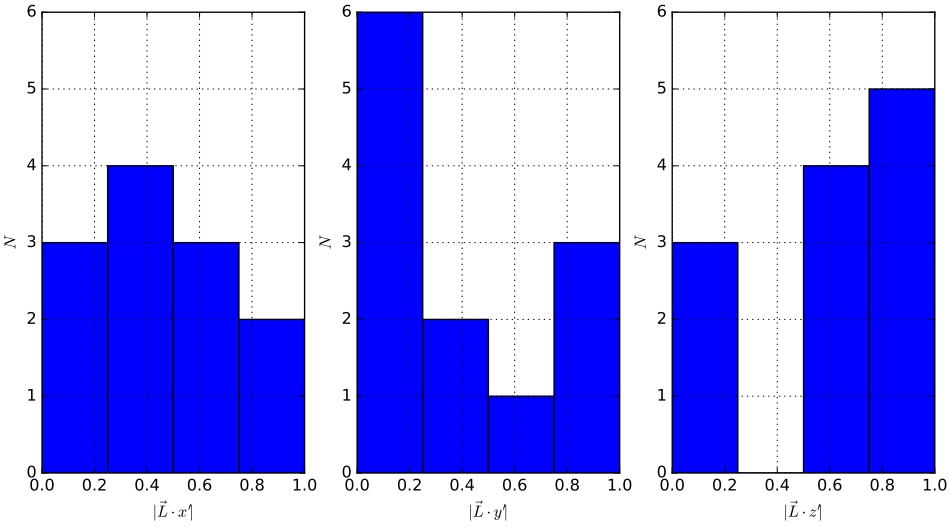

Figure 3.8: Orbital angular momentum vectors in the field galaxy basis, calculated from the midpoint between the two primaries in the each simulation volume. Each plot shows a histogram of the APOSTLE primary orbit angular momenta dotted with the principal axes of each volume.

We see that despite the appearance of non-random distributions, the KS tests against uniformity yield $P_{x'} = 0.50$, $P_{y'} = 0.20$ and $P_{z'} = 0.17$, none of which are significantly unlikely to be the result of random sampling ($P < 0.05$).

In our Local Group, the angular momentum vector of the orbit between the Milky Way and M31 galaxies is estimated to lie at $(l, \beta) = (-161°, 30°)$ with very large uncertainties (Pawlowski et al., 2013[38]).

Figures 3.7 and 3.8 suggest that the present-day distribution of matter has very little correlation with the orientations of the individual galaxies or their orbits.

3.2.5 Comparison of Stellar Disk Angular Momenta

Next, we will compare the relative alignments between the pairs of galaxies in the APOSTLE simulations. We begin with a dot product between the angular momenta of the two primaries' stellar disks in each APOSTLE volume, as shown in Figure 3.9.

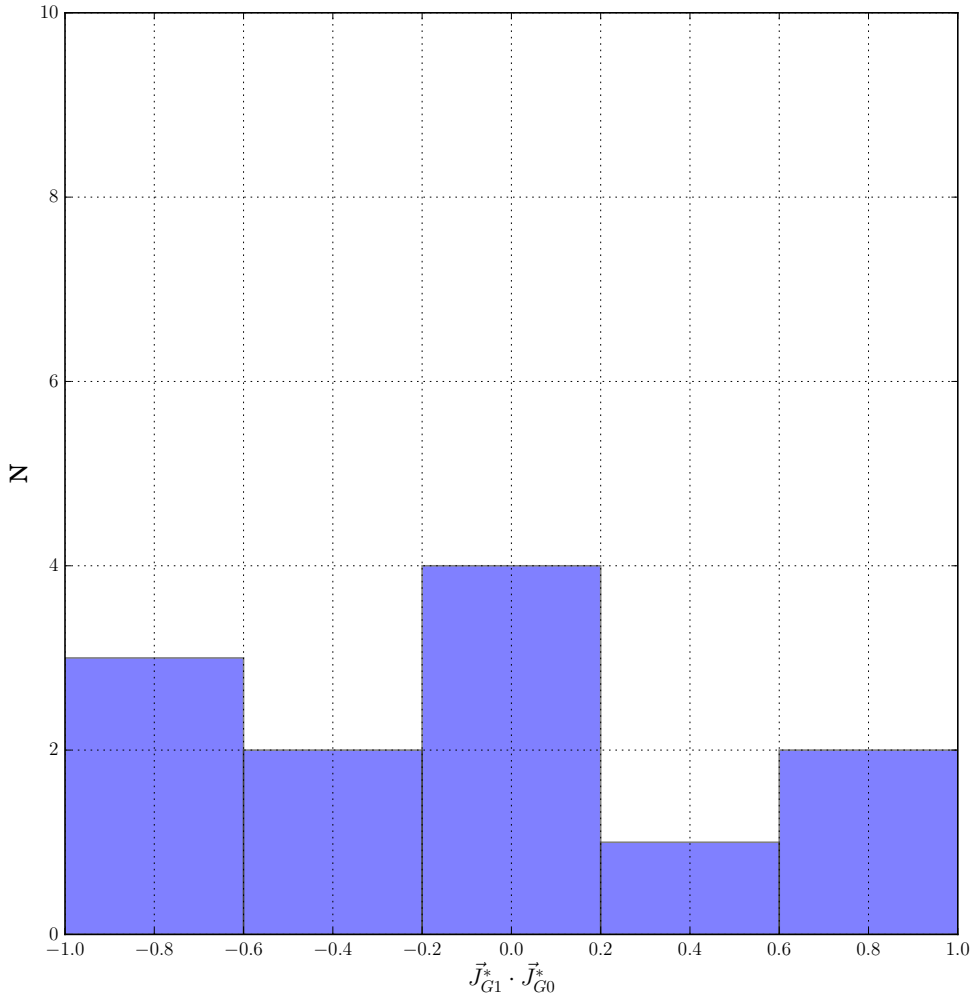

Figure 3.9: Dot products of the angular momentum vectors of the two primary stellar disks for all 12 APOSTLE volumes.

There is no evidence of a non-random distribution ($P_{KS} = 0.72$), which suggests that the stellar disks have no correlation with each other. The dot product between the disks of the Milky Way and M31 galaxies is 0.49.

3.2.6 Comparison of Stellar Disk Angular Momentum with Direction Towards Other Primary Galaxy

Figure 3.10 shows the dot products of the stellar disks of the APOSTLE primaries and the vector towards the other primary in their volume. The distribution is not convincingly different from a random sample ($P_{KS} = 0.67$).

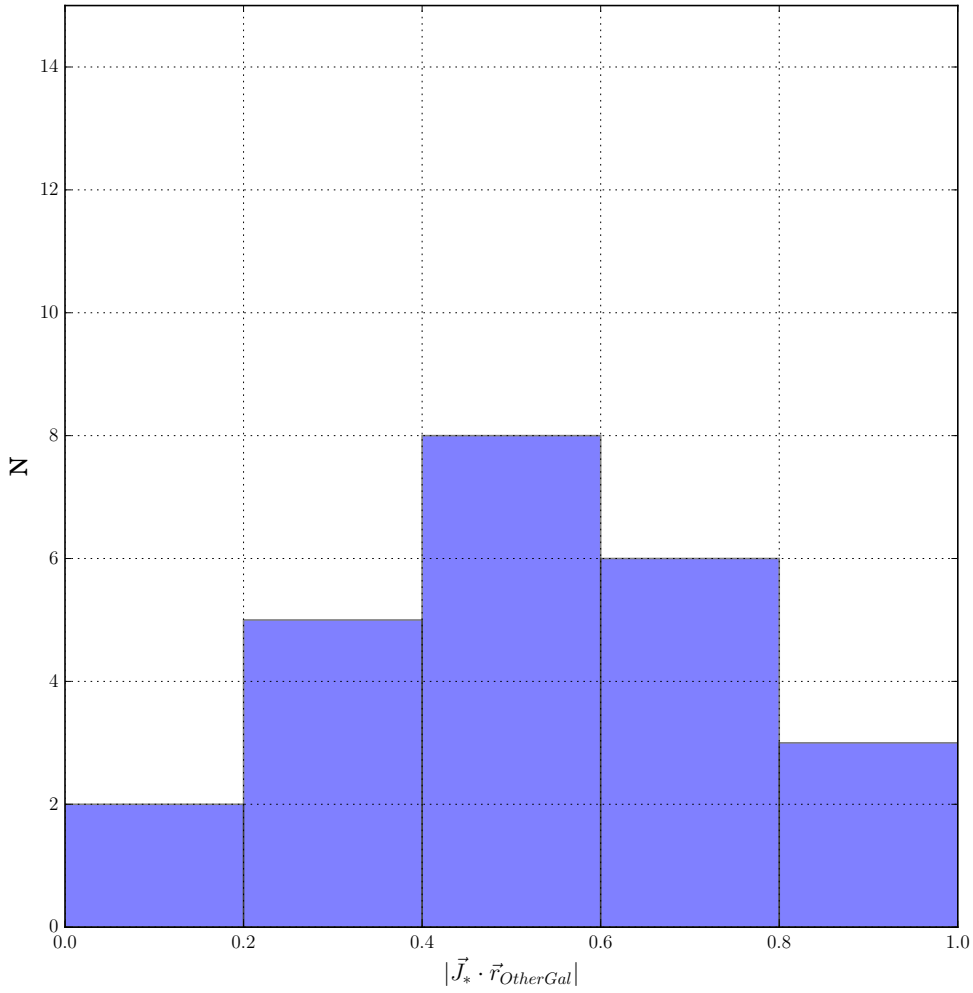

Figure 3.10: Dot product of the stellar disk of a primary galaxy and the vector towards the other primary in that volume.

The Milky Way's angular momentum vector dotted with the direction towards M31 is 0.36, and that of M31 is 0.23, which means that both galaxies are roughly

edge-on to each other.

3.2.7 Comparison of Halo Angular Momenta

Figure 3.11 shows the dot product of the angular momentum vectors between the dark matter halos of the two primary galaxies in each volume. This distribution is significantly non-random ($P_{KS} = 6.0 \times 10^{-3}$), which suggests that nearby massive halos tend to spin counter to each other.

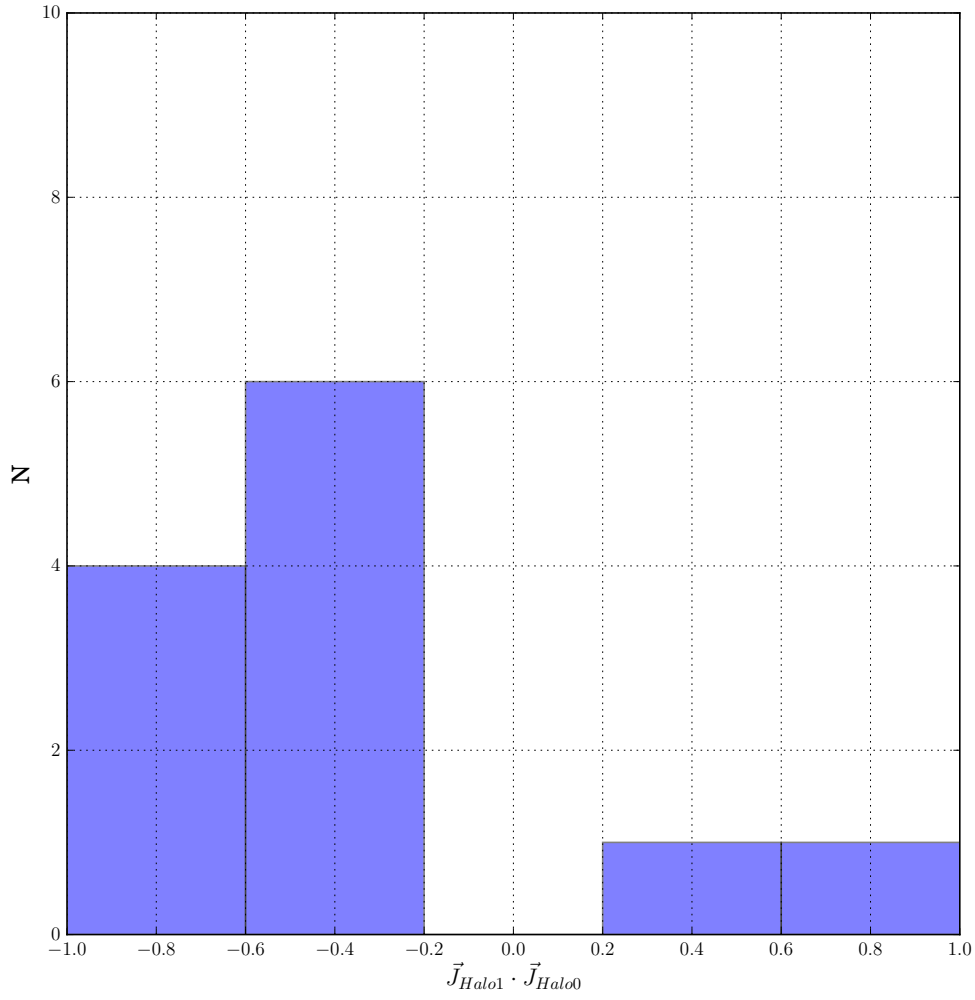

Figure 3.11: Alignment of the halos of the two primary galaxies in each APOSTLE volume.

3.2.8 Comparison of Stellar Disk Angular Momentum with Halo Angular Momentum

Figure 3.12 shows the distribution of dot products between the stellar disks and dark matter halo angular momentum vectors of APOSTLE primary galaxies. This distribution is significantly non-random ($P_{KS} = 6.4 \times 10^{-4}$), which means that stellar disks are biased towards spinning with their dark matter halo.

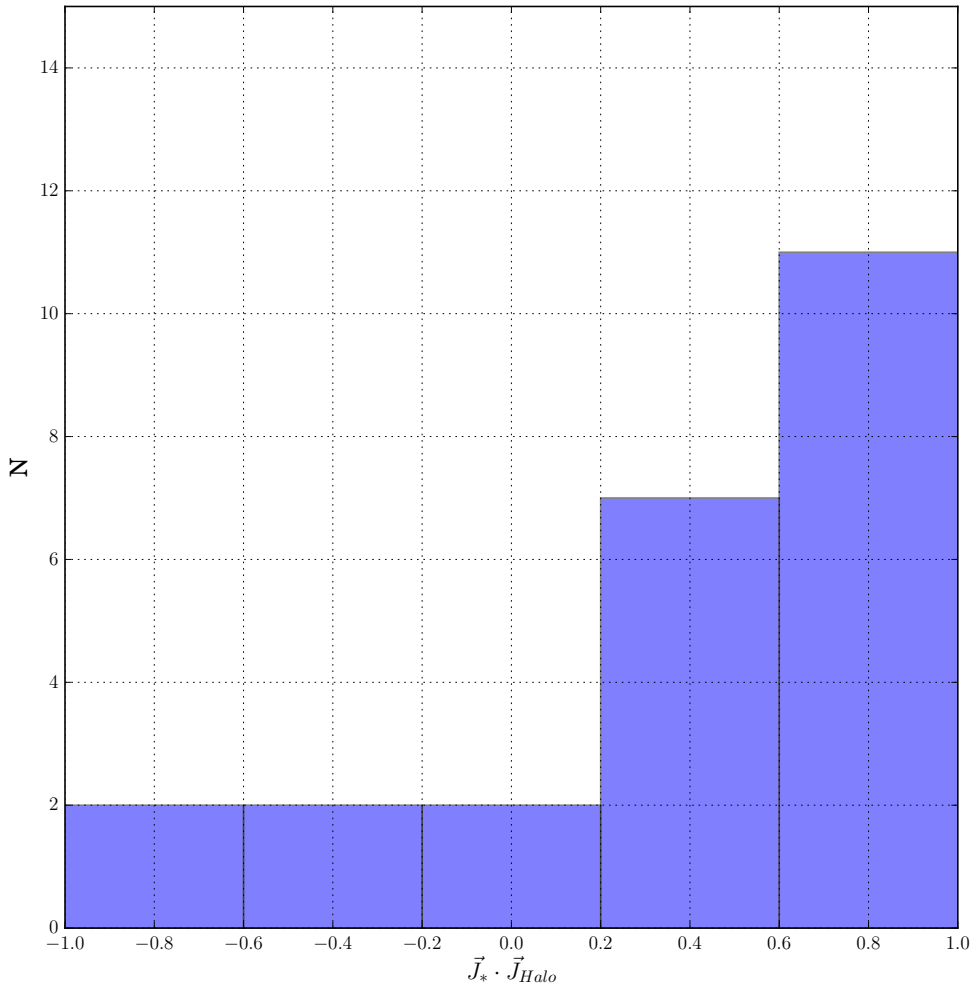

Figure 3.12: Alignment of the stellar disk angular momentum vector with that of its halo.

This result, in combination with Figure 3.11, would suggest that the stellar disk

angular momenta should be anti-aligned, however the scatter in both distributions removes any ability to see a correlation.

3.3 Summary

We have analyzed the anisotropy of the Local Group Field Dwarf distribution, in the context of the APOSTLE simulations, and have determined several features of the Local Group system that appear to be significantly non-random throughout the APOSTLE LG analogues:

- **The anisotropy of the LG field dwarfs compared with the SGP:** The distribution of Local Group field dwarfs is anisotropic, with a minor axis in good alignment with that of the SGP. This result is unchanged even if the completeness of the data is taken into account.
- **The geometry of the LG field dwarf distribution:** The most likely principal axis ratios are $0.7 < \frac{b}{a} < 0.8$, and $0.45 < \frac{c}{b} < 0.7$, with a minor axis at galactocentric $(l, \beta) = (-137.92^\circ \pm 19.50^\circ, -5.27^\circ \pm 1.68^\circ)$.
- **The vector between the two primary galaxies compared to the LG field dwarf distribution:** The vector separating the two major galaxies in the APOSTLE L2 simulations tends to be perpendicular to the minor axis of the field galaxy distribution.
- **The alignment of APOSTLE stellar disk angular momentum vectors with the LG field dwarf distribution:** The angular momentum vectors of the stellar disks of APOSTLE primary galaxies are biased towards alignment along the minor axis of the dwarf galaxy distribution.
- **The alignment of APOSTLE stellar disk angular momentum with that of their host halos:** Many of the APOSTLE galaxies are rotating with their host halos. Those host halos also tend to be anti-aligned with each other. The scatter around these trends means there is no clear bias in alignment between the stellar disks.

Chapter 4

Conclusions

This dissertation examines the spatial distributions of baryons and metals in the Local Group (LG) using numerical simulations. For this, we used the APOSTLE (A Project Of Simulating The Local Environment; Sawala et al., 2015[40]) simulations, which consist of a set of 12 hydrodynamic zoom-in volumes selected from the large DOVE cosmological box (Jenkins, 2013[23]) dark matter-only simulations. These regions were selected to have similar physical and dynamical properties to our observed Local Group (Sawala et al., 2015[40]). These volumes have two primary halos that are isolated from other large structures, each of virial mass $M_{200} \approx 10^{12} M_{\odot}$[1], separated by 500 to 1000 kpc, and approaching each other at between 0 km/s and 250 km/s. These correspond to the Milky Way (MW) and M31 galaxies. The smaller galaxies that exist within 300kpc of either primary galaxy will be referred to as the *satellites* of that primary. Non-satellite galaxies, with (i) $M_{200} > 5 \times 10^9 M_{\odot}$, (ii) Stellar mass $M^* > 10^5 M_{\odot}$, and (iii) that are within 3 Mpc of the MW will be referred to as *LG field dwarfs* in this thesis.

4.1 Inventory of Baryons and Metals in Simulations of the Local Group

4.1.1 Baryons

The baryonic mass contained within large regions of space that are representative of the universe as a whole is given by the values of the cosmological parameters $\Omega_m = 0.272$ and $\Omega_b = 0.0455$ (Komatsu et al., 2011[3]), the fraction of the critical density of the universe made up by all matter, and by baryons, respectively. In a

[1]The virial radius corresponds to the radius that encloses a density of 200 times the critical density of the universe, while the virial mass is the total mass contained within the virial radius.

halo comprised of both dark matter and baryons, the expected cosmological ratio between them is given by $f_b^{exp} = \Omega_b/\Omega_m = 0.167$. On the scale of galaxy clusters, the baryonic mass contained within the virial radius is roughly equal to the expected value, $M_b = f_b \times M_{200}$ (White et al., 1993[31]), henceforth M_b^{exp}. However, the baryon content of smaller scale structures, such as individual galaxies, is estimated by abundance matching (Behroozi et al., 2013[41]) to be far below the cosmological fraction. The Milky Way galaxy, for instance, contains only 20% of the expected baryonic mass and is considered a case where galaxy formation has been quite efficient (Oman et al., 2016[42]). This means that 80% of the the baryons have not made it into the central galaxy, and are either in the halo, or have been ejected outside of the virial radius. Because these baryons are low density and highly ionized, they are difficult to detect. We have used the APOSTLE simulations to examine the total baryonic content of a wide range of halos, with specific focus on the pairs of primary galaxies. We have also characterized the mass and spatial distribution of the gas in the halo of these galaxies, to ascertain the impact this gas has on the total baryonic content of a halo. The findings are summarized below.

- **Baryonic mass as a function of virial mass:** LG field dwarfs and primary galaxies have a lower baryonic mass within their virial radius than expected from the cosmological fraction. (Figure 2.1)

- **Baryonic retention in galaxies of different masses:** The baryonic fraction within a halo increases with mass. From under 10% of M_b^{exp}, at $M_{200} < 10^{10} M_\odot$ to approximately 60%, for the APOSTLE primary galaxies.

- **Baryonic retention in stars:** In APOSTLE, baryonic matter is either in the form of stars or gas. Most of the stars in a galaxy form near the centre of the halo, within a radius of $0.15 \times R_{200}$, which I will refer to as the galactic radius r_{gal}. In APOSTLE primary galaxies, stars compose roughly 15% of M_b^{exp}, on average.

- **Baryonic retention in star-forming gas:** The gas in the halo of an APOSTLE primary galaxy spans a wide range of temperatures and densities (Figure 2.4). Gas that is cool and dense enough to form stars is concentrated within r_{gal}, and accounts for less than 5% of M_b^{exp}.

- **Subpopulations of the circumgalactic medium:** Within a halo, gas that lies beyond the galactic radius but within the virial radius is generally unable to form stars. This non-star-forming gas will be referred to as the circumgalactic medium (CGM). In the case of APOSTLE primaries, it is possible to distinguish two distinct populations of CGM gas. These populations can be differentiated by a temperature cut at $10^5 K$.

- **Baryonic retention in gas above 10^5 K:** CGM gas above this temperature, which I will refer to as the warm-hot CGM (WHCGM), is near the virial temperature of the halo. This WHCGM is roughly in pressure-equilibrium with the gravitational forces of the halo, and has a shallow ($r^{-0.8}$) density profile that extends out to 150 kpc from the centre of the halo, and declines more steeply (r^{-2}) beyond this radius. This reservoir of hot gas accounts for roughly 30% of M_b^{exp} of an APOSTLE primary.

- **Baryonic retention below 10^5 K:** CGM gas with a temperature below $10^5 K$, which I will refer to as the cool CGM (CCGM), is clumpy and infalling. The density profile of the CCGM is also steeper, proportional to r^{-2}. About 10% of M_b^{exp} is held in the CCGM.

These results characterize the baryons that have not been ejected from the virial radius of dark matter halos, and provide estimates of the total mass that has escaped due to feedback. The baryonic masses of individual APOSTLE primary galaxies, and their average, is provided in Table 2.3.

4.1.2 Metals

We have seen that if the total baryonic mass within the virial radius of a primary galaxy is summed, only approximately 60% of M_b^{exp} is recovered. This leaves roughly 40% outside the virial radius of the halo. Why have these baryons been ejected? The most likely culprit is stellar feedback, which is capable of injecting enough energy into the gas of a galaxy for it to escape the virial radius. This mechanism, however, also enriches the gas that remains, so we shall now investigate the distribution of metals between the baryonic components of a galaxy.

The choice of initial mass function (IMF), stellar yields, and stellar lifetimes in the APOSTLE simulations provide a tight relation between total metal mass and

long-lived stellar mass of 5.5%. This gives the total mass of metals that have been produced by the stars within a halo, henceforth M_z^{exp}, and to compare the total metal mass currently within the virial radius with this expected mass. The results follow:

- **Metal mass as a function of stellar mass:** Roughly 70% of the M_z^{exp} of an APOSTLE primary galaxy are retained within its virial radius. This fraction decreases with stellar mass until it becomes constant below $M^* < 10^9 M_\odot$. (Figure 2.7)
- **Metal retention in stars and the CGM:** In primary galaxies, the mass of metals held in the stars is approximately equal to that held in the CGM. This mass makes up approximately 30% of M_z^{exp}.
- **Metal retention in star-forming gas:** In APOSTLE primary galaxies, the star-forming gas contains 10% of M_z^{exp}.
- **Metals in the WHCGM and CCGM:** The metals in the CGM are split evenly between the WHCGM and the CCGM. Because the total mass of the WHCGM is roughly twice that of the CCGM, its metallicity is approximately half. (Figure 2.8)
- **Metal retention in the CGM for low-mass galaxies:** In contrast, for low-mass galaxies, with $M^* < 10^9 M_\odot$, a majority of the metals are held in CGM gas.

As we can see from this accounting, the most massive APOSTLE galaxies eject a lower fraction of produced metals ($\approx 30\%$) than they do baryons ($\approx 40\%$). Using the average numbers from Tables 2.3 and 2.4, the average metallicity of the lost gas is comparable to that of the CGM, which makes up roughly 40% of the M_b^{exp} and 30% of M_z^{exp}.

4.2 The Spatial Distribution of the Local Group Galaxies

Another major topic of this thesis is the spatial distribution of galaxies in the Local Group. The geometry of the LG is characterized by two massive galaxies, and by the surrounding dwarfs. The LG is embedded in a large scale flattened structure that extends out to tens of Mpc, called the Supergalactic Plane (SGP; deVaucouleurs,

1952[36]). Previous work has analyzed how the LG geometry is related to the larger scale SGP structure (Hartwick, 2000[37]; Pawlowski et al., 2013[38]) and reported that they found a similar flattening. We reanalyze these claims with a larger sample of data. We also correct for the observational biases that arise due to the Zone of Avoidance[2] to determine the relation between the local distribution of matter and that of the larger scale structure within which it is embedded.

The selection of Local Group galaxies used in this work comes from the Extragalactic Distance Database (Tully et al., 2009[17]). They were chosen to be within 3 Mpc from the MW, with a stellar mass of $M^* > 10^5 M_\odot$, calculated from the V or B band magnitudes, assuming a mass-to-light ratio of 1 in solar units. Many of these selected galaxies are in close proximity to either the MW or M31 galaxies. Galaxies will be considered satellites if they lie within 300 kpc from either primary. The remaining dwarfs will be referred to as *LG field dwarfs*. The distributions of the satellites and field dwarfs on the sky are shown in Figure 3.1.

To quantify the geometry of the LG field dwarf distribution, we use the unnormalized inertia tensor of the 3D galactocentric coordinates of those galaxies. The eigenvectors of this tensor provide us with the principal axes of this distribution. The directions of these axes, with contours estimating the error due to the zone of avoidance, are shown in Figure 3.4.

These principal axes allow us to define a set of basis vectors that correspond to the spatial properties of the LG field dwarf system. In this basis, the $\hat{x}'$ vector corresponds to the major, the $\hat{y}'$ to the intermediate, and the $\hat{z}'$ to the minor principal axes.

The ratios of the eigenvalues of the inertia tensor give us an idea of the shape of the LG field dwarf distribution. The observed LG field dwarfs form a triaxial distribution, with $b/a \approx 0.7$ and $c/b \approx 0.5$. The correction for the zone of avoidance is small, and shifts the axial ratios to $0.7 < b/a < 0.8$ and $0.45 < c/b < 0.7$, as shown in Figure 3.3.

The results for the observed LG are summarized below.

- **Comparison of the LG $\hat{z}'$ axis with the minor axis of the SGP:** The

[2] a strip of sky within galactocentric latitudes $\beta = \pm 14°$ where galaxy detection is difficult due to absorption by the dust in the MW galaxy.

minor axis of the LG field dwarf distribution is very well aligned ($\approx 5^\circ$ off) with the minor axis of the SGP.

- **The spatial distribution of the MW and M31 galaxies:** The MW and M31 galaxies, which were not directly used to calculate the principal axes, lie very close to the $\hat{x}'$-$\hat{y}'$ plane.

- **The directions of the MW and M31 spin axes:** The MW and M31 have spin axes, defined by their angular momentum vectors. The spin axis of the MW lies on the SGP, while that of M31 lies close to the $\hat{z}'$ axis, with $cos(\vec{J}_{M31}, z') = 0.83$. This corresponds to an angle of 30 degrees.

- **The direction of the MW-M31 orbital axis** The MW-M31 orbital pole is estimated to lie at $(l, \beta) = (-161^\circ, 30^\circ)$, with large uncertainties (Pawlowski et al., 2013[38]). The angle between the $\hat{z}'$ axis and this vector is approximately 40°.

- **The alignment of the MW and M31 spin axes with the vector separating them:** The MW and M31 spin axes are both close to perpendicular to the vector that joins the two galaxies, with $\theta_{MW} \approx 70^\circ$, and $\theta_{M31} \approx 75^\circ$.

As we can see from the results above, the LG field dwarf distribution appears to be an extension of the larger scale structure within which the LG is embedded. We can compare these results with the larger sample found in the 12 realizations of the LG from the APOSTLE project.

4.2.1 The Spatial Distribution of the APOSTLE Local Group Galaxies

For our sample, we use our definition of APOSTLE LG field dwarfs from the first paragraph of this chapter. Since this is an analogous analysis, we will define analogous terms with the same inertia tensor calculation for each simulated volume as in the previous section. These inertia tensors will allow us to define an $\hat{x}'$-$\hat{y}'$-$\hat{z}'$ basis for each simulated volume.

The distributions of APOSTLE LG field dwarfs generally have comparable anisotropy to that of the observed LG (Figure 3.3). The average axial ratios are roughly $b/a \approx 0.7$ and $c/b \approx 0.65$. These values are comparable to those of the observed LG, $b/a \approx 0.7$ and $c/b \approx 0.5$. We cannot check whether the APOSTLE field dwarf distributions

match the larger scale structure from which the volumes were selected, as the resimulated APOSTLE volume is too small for such a comparison.

Our findings are below:

- **The spatial distribution of the APOSTLE primaries:** As in the observations, the two main galaxies generally lie near the $\hat{x}'$-$\hat{y}'$ plane of each volume. (Figure 3.6)

- **The directions of the APOSTLE primaries' spin axes:** We find that in APOSTLE there doesn't appear to be a preference towards alignment with any axis, with the exception of a weak trend towards the z' axis ($P_{random} \approx 0.048$).(Figure 3.7) Only the spin axis of M31, which lies 30° from the observed $\hat{z}'$ axis, follows this trend.

- **The directions of the APOSTLE primaries' orbital axes:** The orbital angular momentum between APOSTLE primaries does not appear to be aligned with any of the principal axes. (Figure 3.8) In the observed LG, this vector lies 40° from the $\hat{z}'$ axis.

- **The alignment of APOSTLE primaries' spin axes and the vector separating them:** In APOSTLE, there is no preference for the angle between the spin vector of a primary galaxy and the direction to the other primary. (Figure 3.10) In the observed LG, the spin axes of both the MW and M31 are nearly perpendicular to the vector between them.

In the simulations, we are also able to check whether there are substantial misalignments between the directions of the spins of the disks and those of the halos in which they are embedded. We find that the disks are generally well-aligned with their halo (Figure 3.12). We also find that the spins of the halos of the two primary galaxies in a volume tend to be rotating in opposite directions (Figure 3.11). This does not, however, translate to a correlation between the spin axes of the stellar disks of primary galaxies, due to the scatter in these relations (Figure 3.9).

These results should provide us with an accurate picture of how we can expect the large scale structure of our local universe to impact the geometry of our Local Group, and the behaviour of its galaxies.

Bibliography

[1] Steigman G. Schramm D. N. Olive K. A. Kang H.-S. Walker, T. P. Primordial nucleosynthesis redux. *Astrophysical Journal*, 376:51–69, 1991.

[2] A. Friedmann. ber die krmmung des raumes. *Zeitschrift fr Physik*, 10:377386, 1922.

[3] K. M.; Dunkley J.; Bennett C. L.; Gold B.; Hinshaw-G.; Jarosik N.; Larson D.; Nolta M. R.; Page L.; Spergel D. N.; Halpern M.; Hill R. S.; Kogut A.; Limon M.; Meyer S. S.; Odegard N.; Tucker G. S.; Weiland J. L.; Wollack E.; Wright E. L. Komatsu, E.; Smith. Seven-year wilkinson microwave anisotropy probe (wmap) observations: Cosmological interpretation. *The Astrophysical Journal Supplement*, 192, 2011.

[4] M. J. White, S. D. M.; Rees. Core condensation in heavy halos: a two-stage theory for galaxy formation and clustering. *Monthly Notices of the Royal Astronomical Society*, 183:341–358, 1978.

[5] P. J. E. Peebles M. Fukugita, C. J. Hogan. The cosmic baryon budget. *The Astrophysical Journal*, 503, 1998.

[6] James M.; de Blok W. J. G.; Zagursky Matthew J. McGaugh, Stacy S.; Schombert. The baryon content of cosmic structures. *The Astrophysical Journal Letters*, 708:L14–L17, 2010.

[7] Aaron A.; Stinson Gregory S.; Macci Andrea V.; Gutcke Thales; Kang Xi Wang, Liang; Dutton. Nihao vii: predictions for the galactic baryon budget in dwarf to milky way mass haloes. *Monthly Notices of the Royal Astronomical Society*, 466:4858–4867, 2017.

[8] J. P. Ostriker R. Cen. Where are the baryons? *The Astrophysical Journal*, 514, 1999.

[9] Jason Tumlinson Molly S. Peeples Todd M. Tripp Andrew J. Fox Nicolas Lehner Christopher Thom John M. O'Meara Amanda Brady Ford Rongmon Bordoloi Neal Katz Nicolas Tejos Benjamin D. Oppenheimer Romeel Dav Jessica K. Werk, J. Xavier Prochaska and David H. Weinberg. The cos-halos survey: Physical conditions and baryonic mass in the low-redshift circumgalactic medium. *The Astrophysical Journal*, 792, 2014.

[10] R. Dav. Missing halo baryons and galactic outflows. *Galaxy Evolution: Emerging Insights and Future Challenges ASP Conference Series*, 419, 2009.

[11] A. Babul P. Madau A. Sokoowska, L. Mayer and S. Shen. Diffuse coronae in cosmological simulations of milky way-sized galaxies. *The Astrophysical Journal*, 819, 2016.

[12] P. Madau L. Mayer J. Guedes, S. Callegari. Forming realistic late-type spirals in a cdm universe: The eris simulation. *The Astrophysical Journal*, 742, 2011.

[13] Robert A.; Bower Richard G.; Furlong Michelle; Schaller Matthieu; Theuns Tom; Dalla Vecchia Claudio; Frenk Carlos S.; McCarthy I. G.; Helly John C.; Jenkins Adrian; Rosas-Guevara Y. M.; White Simon D. M.; Baes Maarten; Booth C. M.; Camps Peter; Navarro Julio F.; Qu Yan; Rahmati Alireza; Sawala Till; Thomas Peter A.; Trayford James Schaye, Joop; Crain. The eagle project: simulating the evolution and assembly of galaxies and their environments. *Monthly Notices of the Royal Astronomical Society*, 446:521–554, 2015.

[14] Benjamin D. Oppenheimer. Deviations from hydrostatic equilibrium in the circumgalactic medium: spinning hot haloes and accelerating flows. *eprint arXiv:1801.00788*, 2018.

[15] Gregory S. Stinson Andrea V. Macci Camilla Penzo Xi Kang Ben W. Keller James Wadsley Liang Wang, Aaron A. Dutton. Nihao project i. reproducing the inefficiency of galaxy formation across cosmic time with a large sample of cosmological hydrodynamical simulations. *Monthly Notices of the Royal Astronomical Society*, 454:8394, 2015.

[16] I. D. KarachentsevO. G. Kashibadze. Masses of the local group and of the m81 group estimated from distortions in the local velocity field. *Astrophysics*, 49:3–18, 2005.

[17] Gurtina; Cox T. J.; Sohn Sangmo Tony; Anderson Jay van der Marel, Roeland P.; Besla. The extragalactic distance database. *The Astrophysical Journal*, 138:323–331, 2009.

[18] Joseph F.; Prochaska J. Xavier; Werk Jessica K. Stern, Jonathan; Hennawi. Simulating the joint evolution of quasars, galaxies and their large-scale distribution. *arXiv:astro-ph/0504097v2*, 2005.

[19] Shy; Springel Volker; Torrey Paul; Sijacki Debora; Xu Dandan; Snyder Greg; Nelson Dylan; Hernquist Lars Vogelsberger, Mark; Genel. Introducing the illustris project: simulating the coevolution of dark and visible matter in the universe. *Monthly Notices of the Royal Astronomical Society*, 444:1518–1547, 2014.

[20] Andrew; Keres Dusan; Faucher-Giguere Claude-Andre; Quataert Eliot; Boylan-Kolchin Michael; Murray Norman; Hayward Christopher C.; Garrison-Kimmel Shea; Hummels Cameron; Feldmann Robert; Torrey-Paul; Ma Xiangcheng; Angles-Alcazar Daniel; Su Kung-Yi; Orr Matthew; Schmitz Denise; Escala Ivanna; Sanderson Robyn; Grudic Michael Y. Hafen Zachary; Kim Ji-Hoon; Fitts Alex; Bullock James S.; Wheeler Coral; Chan T. K.; Elbert Oliver D.; Narananan Desika Hopkins, Philip F; Wetzel. Fire-2 simulations: Physics versus numerics in galaxy formation. *eprint arXiv:1702.06148*, 2017.

[21] James W. Wadsley Benjamin W. Keller Thomas R. Quinn. Gasoline2: a modern smoothed particle hydrodynamics code. *Monthly Notices of the Royal Astronomical Society*, 471:23572369, 2017.

[22] M.; Parry O. H.; Navarro J. F.; Jenkins A.; Springel V.; Teyssier R.; Carlson E.; Couchman H. M. P.; Crain R. A.; Dalla Vecchia C.; Frenk-C. S.; Kobayashi C.; Monaco P.; Murante G.; Okamoto T.; Quinn T.; Schaye J.; Stinson G. S.; Theuns T. Wadsley J.; White S. D. M.; Woods R. Scannapieco, C.; Wadepuhl. The aquila comparison project: the effects of feedback and numerical methods on simulations of galaxy formation. *Monthly Notices of the Royal Astronomical Society*, 423:1726–1749, 2012.

[23] Adrian Jenkins. A new way of setting the phases for cosmological multiscale gaussian initial conditions. *Monthly Notices of the Royal Astronomical Society*, 434:2094–2120, 2013.

[24] Joop; Bower Richard G.; Furlong Michelle; Schaller Matthieu; Theuns Tom; Dalla Vecchia Claudio; Frenk Carlos S.; McCarthy Ian G.; Helly John C.; Jenkins Adrian; Rosas-Guevara Yetli M.; White Simon D. M.; Trayford James W. Crain, Robert A.; Schaye. The eagle simulations of galaxy formation: calibration of subgrid physics and model variations. *Monthly Notices of the Royal Astronomical Society*, 450:1937–1961, 2015.

[25] Volker Springel. The cosmological simulation code gadget-2. *Monthly Notices of the Royal Astronomical Society*, 364:1105–1134, 2005.

[26] Philip F. Hopkins. Pressure-entropy sph: Pressure-entropy smooth-particle hydrodynamics. *Astrophysics Source Code Library*, 2013.

[27] Gilles Chabrier. Galactic stellar and substellar initial mass function. *Publications of the Astronomical Society of the Pacific*, 115:763–795, 2003.

[28] G.; Frenk C. S.; White S. D. M. Davis, M.; Efstathiou. The evolution of large-scale structure in a universe dominated by cold dark matter. *Astrophysical Journal*, 292:371–394, 1985.

[29] Simon D. M.; Tormen Giuseppe; Kauffmann Guinevere Springel, Volker; White. Populating a cluster of galaxies - i. results at z=0. *Monthly Notices of the Royal Astronomical Society*, 328:726–750, 2001.

[30] F.; Krongold Y.; Mathur S.; Elvis M. Nicastro, F.; Senatore. A distant echo of milky way central activity closes the galaxys baryon census. *The Astrophysical Journal Letters*, 828, 2016.

[31] Julio F.; Evrard August E.; Frenk Carlos S. White, Simon D. M.; Navarro. The baryon content of galaxy clusters: a challenge to cosmological orthodoxy. *Nature*, 366:429–433, 1993.

[32] Christopher Thom Jason Tumlinson Todd M. Tripp John M. O'Meara Jessica K. Werk, J. Xavier Prochaska and Joseph D. Meiring. The cos-halos survey: Keck lris and magellan mage optical spectroscopy. *The Astrophysical Journal Supplement Series*, 198, 2012.

[33] R. L.; van Hoof P. A. M.; Williams R. J. R.; Abel N. P.; Lykins M. L.; Shaw G.; Henney W. J.; Stancil P. C. Ferland, G. J.; Porter. The 2013 release of cloudy. *Revista Mexicana de Astronoma y Astrofsica*, 49:137–163, 2013.

[34] Joseph F.; Prochaska J. Xavier; Werk Jessica K. Stern, Jonathan; Hennawi. A universal density structure for circumgalactic gas. *The Astrophysical Journal*, 830, 2016.

[35] Andreea S. Font Joop Schaye Tom Theuns Mara Emilia De Rossi, Richard G. Bower. Galaxy metallicity scaling relations in the eagle simulations. *Monthly Notices of the Royal Astronomical Society*, 472:33543377, 2017.

[36] G. de Vaucouleurs. Evidence for a local supergalaxy. *The Astronomical Journal*, 58:30–32, 1952.

[37] F. D. A. Hartwick. The structure of the outer halo of the galaxy and its relationship to nearby large-scale structure. *The Astronomical Journal*, 119, 2000.

[38] Pavel; Jerjen Helmut Pawlowski, Marcel S.; Kroupa. Dwarf galaxy planes: the discovery of symmetric structures in the local group. *Monthly Notices of the Royal Astronomical Society*, 435:1928–1957, 2013.

[39] Ofer Lahav Renee C. Kraan-Korteweg. The universe behind the milky way. *The Astronomy and Astrophysics Review*, 10:211261, 2000.

[40] Till Sawala Carlos S. Frenk Azadeh Fattahi Julio F. Navarro Richard G. Bower Robert A. Crain Claudio Dalla Vecchia Michelle Furlong John. C. Helly Adrian Jenkins Kyle A. Oman Matthieu Schaller Joop Schaye Tom Theuns James Trayford Simon D. M. White. The apostle simulations: solutions to the local group's cosmic puzzles. *Monthly Notices of the Royal Astronomical Society*, 457:19311943, 2015.

[41] Risa Wechsler Adam Muzzin Casey Papovich Mauro Stefanon Peter Behroozi, Danilo Marchesini. Using cumulative number densities to compare galaxies across cosmic time. *The Astrophysical Journal Letters*, 777, 2013.

[42] Laura V. Sales Azadeh Fattahi Carlos S. Frenk Till Sawala Matthieu Schaller Simon D. M. White Kyle A. Oman, Julio F. Navarro. Missing dark matter in dwarf galaxies? *Monthly Notices of the Royal Astronomical Society*, 460:36103623, 2016.